



Constraining lowermost mantle anisotropy with body waves: A synthetic modeling study

Journal:	<i>Geophysical Journal International</i>
Manuscript ID	GJI-S-18-0612.R1
Manuscript Type:	Research Paper
Date Submitted by the Author:	06-Nov-2018
Complete List of Authors:	Creasy, Neala; Yale University, Department of Geology and Geophysics Pisconti, Angelo; Westfälische Wilhelms-Universität Münster Institut für Geophysik Long, Maureen; Yale University, Geology and Geophysics; Thomas, Christine; Westfälische Wilhelms-Universität Münster Institut für Geophysik Wookey, James; University of Bristol, School of Earth Sciences
Keywords:	Seismic anisotropy < SEISMOLOGY, Composition and structure of the mantle < COMPOSITION and PHYSICAL PROPERTIES, Mantle processes < GENERAL SUBJECTS, Statistical seismology < SEISMOLOGY

1
2
3
4
5
6
7
8
9
10
11
12
13
14
15
16
17
18
19
20
21
22
23
24
25
26
27
28
29
30
31
32
33
34
35
36
37
38
39
40
41
42
43
44
45
46
47
48
49
50
51
52
53
54
55
56
57
58
59
60

Constraining lowermost mantle anisotropy with body waves: A synthetic modeling study

Neala Creasy^{1*}, Angelo Pisconti², Maureen D. Long¹, Christine Thomas², and James Wookey³

¹Department of Geology and Geophysics, Yale University

²Institut für Geophysik, Universität Münster

³Department of Earth Sciences, University of Bristol

*Corresponding author. Email: neala.creasy@yale.edu

1
2
3 15 Summary
4

5
6 16 Different mechanisms have been proposed as explanations for seismic anisotropy
7
8 17 at the base of the mantle, including crystallographic preferred orientation of various
9
10 18 minerals (bridgmanite, post-perovskite, and ferropericlase) and shape preferred orientation
11
12 19 of elastically distinct materials such as partial melt. Investigations of the mechanism for
13
14 20 D" anisotropy usually yield ambiguous results, as seismic observations rarely (if ever)
15
16 21 uniquely constrain a mechanism or orientation and usually rely on significant assumptions
17
18 22 to infer flow patterns in the deep mantle. Observations of shear wave splitting and polarities
19
20 23 of SdS and PdP reflections off the D" discontinuity are among our best tools for probing
21
22 24 D" anisotropy; however, currently available datasets cannot constrain one unique scenario
23
24 25 among those suggested by the mineral physics literature. In this work, we determine which
25
26 26 body wave observations (e.g. SKS, SKKS, and ScS) are required to uniquely constrain a
27
28 27 mechanism for D" anisotropy via a forward modeling approach. We test multiple models
29
30 28 based on single-crystal and polycrystalline elastic tensors provided by mineral physics
31
32 29 studies. Our modeling predicts fast shear wave splitting directions for SKS, SKKS, and
33
34 30 ScS phases, as well as polarities of P and S wave reflections off the D" interface, for a
35
36 31 range of propagation directions, via solution of the Christoffel equation. We run tests using
37
38 32 randomly selected synthetic datasets based on a given starting model, controlling the total
39
40 33 number of measurements, the azimuthal distribution, and the type of seismic phases. For
41
42 34 each synthetic dataset, we search over all possible elastic tensors and orientations to
43
44 35 determine which are consistent with the synthetic data. Overall, we find it difficult to
45
46 36 uniquely constrain the mechanism for anisotropy with a reasonable number of seismic
47
48 37 anisotropy measurements (based on currently available studies) with only one
49
50
51
52
53
54
55
56
57
58
59
60

1
2
3 38 measurement technique (SKS, SKKS, ScS, or reflection polarities). However, datasets that
4
5 39 include SKS, SKKS, and ScS measurements, or a combination of shear wave splitting and
6
7
8 40 reflection polarity measurements, dramatically increase the probability of uniquely
9
10 41 constraining the starting model and its orientation (by nearly 60% on average). Based on
11
12 42 these findings, we identify specific regions of the lowermost mantle with sufficient raypath
13
14
15 43 coverage for a combination of measurement techniques.
16
17
18
19
20
21
22
23
24
25
26
27
28
29
30
31
32
33
34
35
36
37
38
39
40
41
42
43
44
45
46
47
48
49
50
51
52
53
54
55
56
57
58
59
60

1
2
3 44 Abbreviated Title: Constraining lowermost mantle anisotropy
4
5
6 45
7
8 46 Keywords (up to 6):
9

10 47 • Seismic anisotropy
11

12 48 • Composition and structure of the mantle
13

14 49 • Mantle processes
15

16 50 • Statistical seismology
17
18
19
20
21
22
23
24
25
26
27
28
29
30
31
32
33
34
35
36
37
38
39
40
41
42
43
44
45
46
47
48
49
50
51
52
53
54
55
56
57
58
59
60

51 1. Introduction

52 Mantle convection finds its surface expression in plate tectonics and represents a
53 crucial dynamic process in the deep Earth. Despite its importance, the pattern of mantle
54 convection and the forces that drive mantle flow remain imperfectly understood. This is
55 particularly true for the deepest mantle: flow at the base of the mantle likely plays an
56 important role in controlling mantle processes and likely influences (and/or is influenced
57 by) structures such as large low shear velocity provinces (LLSVPs). **Subducting slabs**
58 **likely penetrate into the lower mantle and hot mantle plumes generate from or near the**
59 **LLSVPs, indicating a strong connection between the surface and deep mantle processes**
60 **(e.g., Garnero et al., 2016).**

61 Observations of seismic anisotropy have the potential to illuminate mantle flow,
62 due to the relationship between strain due to mantle convection and seismic anisotropy via
63 lattice preferred orientation (LPO) or shape preferred orientation (SPO) mechanisms. The
64 presence of anisotropy in the D" layer at the base of the mantle has been known for several
65 decades (e.g., Lay and Helmberger, 1983) from the analysis of body wave phases (as
66 summarized in Nowacki et al., 2011). **At this point a relatively small fraction (Figure 1) of**
67 **the core mantle boundary region has been explored for D" anisotropy using body waves.**
68 **Figure 1 shows a map, updated from Nowacki et al. (2011) illustrating the geographical**
69 **coverage of previous studies (including recent work by Creasy et al., 2017, Deng et al.,**
70 **2017, Simmons et al., 2015, Ford et al., 2015, Long and Lynner, 2015, Lynner and Long,**
71 **2014, Cottaar and Romanowicz, 2013, and Thomas et al., 2011). Despite these**
72 **observations, however, we still do not fully understand the anisotropy in these regions.**
73 **Several different models for D" anisotropy have been proposed, including those that invoke**

1
2
3 74 LPO of bridgmanite (Br), post-perovskite (Ppv), or ferropericlae (Fp), and those that
4
5 75 invoke SPO of partial melt (see Nowacki et al., 2011 for a review). The mechanism(s)
6
7 76 responsible for D" anisotropy, the dominant slip systems of these mechanism(s), the
8
9 77 orientation of the anisotropic fabric, and the implications for mantle flow geometries thus
10
11
12 78 remain poorly understood.

13
14
15 79 A variety of body waves has been used to study anisotropy in the deepest mantle.
16
17 80 Specifically, direct S, ScS, and Sdiff have been used to observe lowermost mantle
18
19 81 anisotropy by measuring shear wave splitting (e.g., Wookey et al., 2005a, Cottaar and
20
21 82 Romanowicz, 2013, Thomas et al., 2007, Ford et al., 2006). Combinations of phases, such
22
23 83 as SKS-SKKS (e.g., Wang and Wen, 2007; Long, 2009) or S-ScS (e.g., Wookey et al.,
24
25 84 2005a; Nowacki et al., 2010), are often useful to isolate the lowermost mantle contribution
26
27 85 to splitting. Thomas et al. (2011) used an array analysis technique to observe reflected P
28
29 86 and S waves off the D" discontinuity; the azimuthal dependence of the polarity of D"
30
31 87 reflections SdS and PdP contains information about lowermost mantle anisotropy. While
32
33 88 body wave observations have been extensively used to study anisotropy at the base of the
34
35 89 mantle, such studies suffer from the fundamental limitation of small azimuthal coverage;
36
37 90 most studies are essentially restricted to a single raypath, which means that the geometry
38
39 91 of anisotropy cannot be tightly constrained.

40
41
42 92 Several recent studies of deep mantle anisotropy have ameliorated this limitation
43
44 93 by targeting regions of D" that are sampled by body waves over multiple azimuths (pink
45
46 94 regions in Figure 1). These include studies of the lowermost mantle beneath Siberia
47
48 95 (Wookey and Kendall, 2008; Thomas et al., 2011), North America (Nowacki et al., 2010),
49
50 96 the Afar region of Africa (Ford et al., 2015), and Australia and New Zealand (Creasy et al.,
51
52
53
54
55
56
57
58
59
60

1
2
3 97 2017). In some cases, **one can** test whether the observations could clearly distinguish
4
5 98 among different mechanisms for anisotropy. For example, Ford et al. (2015) and Creasy et
6
7
8 99 al. (2017) carried out forward modeling of ScS, SKS, and SKKS splitting datasets over
9
10 100 multiple azimuths to test whether a unique mechanism for anisotropy and/or a unique
11
12 101 orientation of **an assumed mechanism** could be identified. In each of these studies it was
13
14 102 found that LPO of Ppv **matches** the observations, but other mechanisms (such as LPO of
15
16
17 103 Br or Fp) were also consistent with the data. **None of the studies summarized in Figure 1**
18
19 104 **has successfully identified a uniquely constrained mechanism or orientation for anisotropy.**
20
21 105 **Motivated by this, we attempt here to understand what observations are needed to**
22
23
24 106 **distinguish the various possible models for D'' anisotropy.**

25
26 107 The goal of this study is to understand what types of body wave datasets (**SKS,**
27
28 108 **SKKS, ScS, and reflection polarities**) are necessary to uniquely constrain the mechanism
29
30
31 109 and geometry of anisotropy in the lowermost mantle using observations of shear wave
32
33 110 splitting and D'' reflection polarities. **Such an understanding** will aid in the design of future
34
35 111 observational studies **to maximize the chances of uniquely constraining a mechanism.** We
36
37 112 are interested in understanding the characteristics of datasets that are best suited to
38
39
40 113 constrain the details of D'' anisotropy, including the number of measurements needed, the
41
42 114 optimal azimuthal coverage, and the optimal combinations of body wave phases. We
43
44 115 **address** two specific questions: 1) What types of datasets (**potentially including SKS,**
45
46 116 **SKKS, and/or ScS splitting, and/or reflection polarities**) are needed to uniquely identify
47
48 117 the causative mechanism for anisotropy (e.g., LPO of Ppv, Br, Fp, or SPO of partial melt)?
49
50
51 118 and 2) if we assume that the mechanism for anisotropy is known to be LPO of Ppv, what
52
53
54 119 type of datasets are needed to uniquely constrain the orientation of the anisotropy?
55
56
57
58
59
60

1
2
3 | 120 We carry out forward modeling tests for a suite of synthetic body wave data. Our
4
5 | 121 approach to forward modeling of synthetic datasets follows our previous work on
6
7 | 122 observations of shear wave splitting in D'' (Ford et al., 2015; Creasy et al., 2017) and also
8
9 | 123 incorporates measurements of D'' polarities of P and S wave reflections (Thomas et al.,
10
11 | 124 2011a). Our approach is to test a variety of candidate elastic tensors that describe various
12
13 | 125 mechanisms for lowermost mantle anisotropy. For each model, we randomly generate more
14
15 | 126 than 5,000 unique synthetic datasets (for SKS, SKKS, and ScS shear wave splitting, plus
16
17 | 127 PdP and SdS polarities) with a certain set of characteristics (e.g., number and type of
18
19 | 128 measurements, as described below) and a random azimuthal distribution. For each set of
20
21 | 129 random raypaths, we compute a set of predicted “observations” of shear wave splitting
22
23 | 130 and/or reflection polarities using a ray theoretical approach. We then attempt to determine
24
25 | 131 what characteristics of body wave datasets are optimal for uniquely constraining anisotropy
26
27 | 132 in the lowermost mantle.
28
29
30
31
32

33
34 | 133

35 | 134 **2. Methods**

36 | 135 2.1 Candidate models for D'' anisotropy

37
38 | 136 We first consider which plausible models for D'' anisotropy should be tested. The
39
40 | 137 lower mantle is likely composed of pyrolite (e.g., Lee et al., 2004), a model composition
41
42 | 138 that consists of ~76 mol% of bridgmanite (Br: MgSiO₃), ~17 mol% of periclase (Fp:
43
44 | 139 (Mg,Fe)O), and ~7 mol% of calcium perovskite (Capv: CaSiO₃). In the D'' layer at the base
45
46 | 140 of the mantle, we expect a phase change of Br to post-perovskite (Ppv: MgSiO₃) (e.g.,
47
48 | 141 Murakami et al., 2004). Based on *ab initio* calculations and laboratory experiments, Br, Fp,
49
50 | 142 and Ppv all have strong single-crystal anisotropy, with Fp being the weakest mineral and
51
52
53
54
55
56
57
58
59
60

1
2
3 143 the most anisotropic (as summarized in Nowacki et al., 2011), although it is volumetrically
4
5 144 less important than Br/Ppv. This suggests that LPO development in any of the dominant
6
7
8 145 lowermost mantle minerals may contribute to the observed anisotropy, as long as
9
10 146 deformation is taking place in the dislocation creep regime (e.g., McNamara et al., 2001).
11
12 147 Another possible mechanism is aligned pockets of an elastically distinct material such as
13
14 148 partial melt in configurations such as disks, tubes, or sheets, creating shape preferred
15
16 149 orientation (SPO) (e.g., Kendall and Silver, 1998) (Tables 1 and 2). .

19 150 We test a suite of models that describe single-crystal elasticity of lowermost mantle
20
21 151 materials derived from *ab initio* calculations, following our previous modeling work (Ford
22
23 152 et al., 2015; Creasy et al., 2017). This approach assumes that an aggregate will have the
24
25 153 same anisotropic geometry (although not strength) as a single crystal. In addition to the
26
27 154 single-crystal models, we test one model (for Fp LPO) based on deformation experiments
28
29
30 155 (Long et al., 2006) and models that invoke the SPO (shape-preferred orientation) of partial
31
32 156 melt (Table 1), with elastic constants calculated using an implementation of effective
33
34 157 medium theory within the MSAT toolbox (Walker and Wookey, 2012).

37 158 Finally, our last candidate model approximates a textured Ppv aggregate and is
38
39 159 derived from a 3D, global mantle flow field calculation in combination with a visco-plastic
40
41 160 self-consistent model LPO development in Ppv (Walker et al., 2011). We determined a
42
43 161 representative elastic tensor for Ppv texture development in high-strain simple shear by
44
45 162 querying the TX2008.V1.P010 model of Walker et al. (2011), which combined a lower
46
47 163 mantle viscosity model from Mitrović and Forte (2004) with a mantle density model from
48
49 164 Simmons et al. (2009). We only considered the case in which slip on the (010) plane
50
51 165 dominates; this is the most likely slip plane for Ppv based on experiments (Walte et al.,
52
53
54
55
56
57
58
59
60

1
2
3 166 2009; Yamazaki et al., 2006), modeling (Goryaeva et al., 2017), and observations of D"
4
5 167 anisotropy (Creasy et al., 2017; Ford et al., 2015; Thomas et al., 2011). To obtain a
6
7 168 representative average tensor for simple shear, we identified a 15° by 15° geographical
8
9 169 region of the global flow (beneath the northern Atlantic Ocean) that is dominated by strong
10
11 170 horizontal shear. We then extracted the 16 elastic tensors (the model calculated tensors
12
13 171 every 5°) from the resulting TX2008.V1.P010 elasticity predictions in this region averaged
14
15 172 them.
16
17
18
19 173

20 174 2.2 Computation of reflection polarities and fast splitting directions

21
22 175 Given the full suite of candidate models for elasticity in D'' to be used in our study
23
24 176 (Table 1), we implement methods for predicting various types of body wave observations
25
26 177 for these scenarios. We calculated predicted shear wave splitting fast directions for SKS,
27
28 178 SKKS, and ScS phases (Figure 2) over a range of azimuths (every 5°) and inclinations for
29
30 179 each of these models (Tables 1) by solving the Christoffel equation (using the MSAT
31
32 180 toolkit of Walker and Wookey [2012]). The three different phases propagate at different
33
34 181 inclination angles: ~55°, 35°, 0° from the horizontal, respectively.
35
36
37
38
39

40 182 We then calculated the reflection polarities of SdS and PdP and the corresponding
41
42 183 predicted shear wave splitting fast directions (Figure 3) over a range of azimuths (every
43
44 184 5°) and inclinations for each of these models (Tables 1 and 2). Table 2 summarizes the
45
46 185 models used to generate predictions of D'' reflection polarities (SdS and PdP), including
47
48 186 the assumed slip system, based on the methodology of Thomas et al. (2011). These models
49
50 187 were constructed by assuming horizontal simple shear at the base of the mantle, where the
51
52 188 dominant slip direction aligns parallel to the CMB, the slip plane is assumed to be
53
54
55
56
57
58
59
60

1
2
3 189 horizontal, and 12% of the aligned single crystals are mixed linearly with its isotropic
4
5 190 equivalent. (This choice of 12% alignment was based on the previous work of Thomas et
6
7
8 191 al. (2011), and yields reasonable anisotropic strengths; since we focus on reflection
9
10 192 polarities and not amplitudes, however, this choice of value is not critical.) We assume that
11
12 193 the aligned grains are sub-parallel with the slip direction and the slip plane is sub-parallel
13
14 194 to the CMB and the remaining grains are randomly oriented for Models A, B, and C (Figure
15
16
17 195 3). We tested three models (Models A [Ppv], C [Br], and D [Fp] in Table 2) in which the
18
19 196 D" discontinuity represents a change in alignment of the mineral grains from an isotropic
20
21 197 (above the discontinuity) to an anisotropic (below the discontinuity) regime. In Model B,
22
23 198 the D" discontinuity is an isotropic phase transformation from Br to anisotropic Ppv. The
24
25 199 predicted values for reflection polarities for each model are shown in Figure 3 and were
26
27 200 calculated using Guest and Kendall (1993) from the velocity perturbation and reflection
28
29 201 coefficients at the interface between an isotropic and anisotropic layer with respect to
30
31
32 202 azimuth from the dominant slip direction and epicentral distance (Thomas et al., 2011).

33
34
35 203 Our approach to calculating predicted shear wave splitting parameters (and
36
37 204 reflection polarities) for our synthetic models makes several simplifying assumptions.
38
39 205 First, we only directly model shear wave splitting due to lowermost mantle anisotropy, and
40
41 206 ignore any potential contributions from the upper mantle. Our approach therefore assumes
42
43 207 that any upper mantle contribution (in real data) has been correctly accounted for; we
44
45 208 further assume that the bulk of the lower mantle is isotropic (Meade et al., 1995). We do
46
47 209 not explicitly consider how incorrect upper mantle corrections could bias the resulting D"
48
49 210 observations, which is beyond the scope of our study. Second, we rely on ray theory and
50
51 211 do not consider finite frequency wave effects in our modeling. Ray theoretical predictions
52
53
54
55
56
57
58
59
60

1
2
3 212 are likely to be generally accurate (e.g., Nowacki and Wookey, 2016), although they may
4
5 213 break down for laterally heterogeneous anisotropic models. Third, in our modeling we
6
7 214 approximate the propagation directions for SKS and SKKS with average inclination angles
8
9 215 for these phases, and for ScS we assume that propagation is horizontal through the D''
10
11 216 layer. This assumption follows previous work (Nowacki et al., 2010; Ford et al., 2015;
12
13 217 Creasy et al., 2017; see Creasy et al., 2017, for a detailed discussion of this point). We
14
15 218 assume the three different phases (SKS, SKKS, and ScS) propagate at different inclination
16
17 219 angles: $\sim 55^\circ$, 35° , 0° from the horizontal, respectively. (Values for straight-line
18
19 220 approximation propagation directions were calculated using TauP (Crotwell et al., 1999)
20
21 221 based on the PREM Earth model (Dziewonski and Anderson, 1980) for distances of 90° -
22
23 222 120° for SKS/SKKS and 60° - 80° for ScS with an event at a depth 10 km.) We use these
24
25 223 average propagation angles for SKS and SKKS in our modeling for simplicity, although
26
27 224 for real data they can vary by up to 10° - 20° from these average values.
28
29
30
31
32
33
34

35 226 2.3 Modeling approach and strategy

36
37 227 Our goal is to conduct a series of stochastic forward modeling simulations to test
38
39 228 whether we can uniquely constrain a given starting model (an elastic tensor) and its
40
41 229 orientation using a dataset with a given set of characteristics (e.g., number and type of
42
43 230 measurements, azimuthal distribution). Our forward modeling framework follows Ford et
44
45 231 al. (2015), who modeled a shear wave splitting dataset that samples the lowermost mantle
46
47 232 beneath the Afar peninsula along the edge of the African LLSVP. We did not consider
48
49 233 delay times in our modeling. Individual delay time measurements contain larger error bars,
50
51 234 which limit the utility of using the relative travel times in a dataset as a discriminant. The
52
53
54
55
56
57
58
59
60

1
2
3 235 complete tradeoff between fabric strength and layer thickness also limits the utility of using
4
5 236 absolute travel times as a constraint.
6
7

8 237 For each of our modeling experiments, we first choose a starting model and
9
10 238 orientation from the possibilities listed in Table 1 (for example, a horizontally aligned
11
12 239 elastic tensor of Ppv, with [100] and [010] axes parallel to the CMB, which we will use to
13
14 240 illustrate our approach in several of the following figures). Second, we randomly identify
15
16 241 a set of raypaths of SKS, SKKS, and/or ScS (sometimes in combination with SdS and PdP
17
18 242 reflection polarities). Third, we calculate the predicted fast-axis directions and/or reflection
19
20 243 polarities of SdS and PdP for each raypath, as described in Section 2.2.
21
22
23

24 244 In the fourth step, we model the synthetic dataset by applying the same forward
25
26 245 modeling technique that we typically use for real data (Ford et al., 2015). Specifically, we
27
28 246 treat the synthetic observations as though the actual model used to generate them was not
29
30 247 known, and test all possible models listed in Tables 1 and 2) in all possible orientations
31
32 248 (every 5°) to identify models/orientations that are consistent with the synthetic dataset. A
33
34 249 candidate model/orientation is discarded if misfits between the predicted and “observed”
35
36 250 fast splitting directions exceed 20° or if the predicted reflection polarities are opposite those
37
38 251 of the “observations”. We apply this 20° cutoff for the splitting observations, based on
39
40 252 reasonable estimates of errors in shear wave splitting studies (see Ford et al., 2015). (While
41
42 253 this misfit criterion is appropriate for measurement errors, it does not take into account
43
44 254 effects such as inaccurate upper mantle corrections for actual D” anisotropy observations,
45
46 255 or the possible finite-frequency effects of complex structure. Explicit consideration of these
47
48 256 effects in D” anisotropy studies is a subject of ongoing research.). For each candidate
49
50 257 model/orientation that was considered an acceptable fit to the synthetic data, we calculated
51
52
53
54
55
56
57
58
59
60

1
2
3 258 a total misfit value (for the fast polarization directions only) based on a residual sum of
4
5 259 squares approach, following Ford et al. (2015). Each fast direction misfit is normalized by
6
7
8 260 the maximum residual of 90° and summed by using the residual sum of squares, in which
9
10 261 we calculate the square of the difference between the observation and data prediction.

11
12 262 The fifth and final step in our modeling strategy is to repeat the entire process a
13
14 263 large number (M) of times, which effectively generates a large number of random raypath
15
16 264 configurations. All of these steps are illustrated in Figure 4. In each iteration, we randomly
17
18
19 265 choose a new azimuthal distribution of raypaths for a new synthetic dataset with varying
20
21 266 characteristics (such as the number and type of observations, described in more detail
22
23 267 below). Consideration of a large number of synthetic datasets, in a stochastic approach,
24
25
26 268 allows us to understand the kind of datasets that are more useful in distinguishing
27
28 269 mechanisms and orientations of anisotropy, by querying a large number of possible datasets
29
30
31 270 with different (random) azimuthal coverage. We report our results by considering what
32
33 271 percentage of the M iterations (each with a randomly generated raypath configuration)
34
35 272 could uniquely identify the starting model. Each individual iteration was designated as
36
37 273 “uniquely constrained” if it successfully identified the correct starting model, and could
38
39 274 completely rule out any other candidate model. However, if there was at least one other
40
41 275 anisotropy configuration (any candidate elastic tensor model, in any orientation) was found
42
43 276 to be consistent with the synthetic observations, that iteration was designated “not uniquely
44
45 277 constrained.” Therefore, all our model results are characterized through a %-uniquely
46
47 278 constrained value, which identifies how what percentage of the M simulations could
48
49
50
51 279 uniquely constrain the starting model.
52
53
54
55
56
57
58
59
60

280 Within this modeling framework, we tested a series of synthetic dataset
 281 characteristics described the following three distinct variables: the number of
 282 measurements (N), ratio of the number of SK(K)S (that is, SKS plus SKKS) measurements
 283 to the total number of shear wave splitting measurements (we term this ratio the “SKS
 284 number”), and the azimuthal distribution of measurements, as quantified by the angular
 285 dispersion (R). Angular dispersion is defined as:

$$286 \quad C_P = \sum_{i=1}^n \cos(a_i), \quad S_P = \sum_{i=1}^n \sin(a_i), \quad (1)$$

$$287 \quad R = \sqrt{C_P^2 + S_P^2}, \quad (2)$$

288 where a_i is a vector of directions and R is angular dispersion, which varies from 0
 289 (uniform dispersion) to 1 (concentration in one direction) (Mardia and Jupp, 2000). A
 290 graphical definition of R is shown in Supplementary Figure S1.

291 We tested different combinations of N and SKS number to gain insight into how
 292 many measurements, and in what combination, are typically needed to uniquely constrain
 293 the anisotropy. For angular dispersion, we calculated the value of R for each of the M
 294 iterations carried out in each test; then, we queried the large number of simulations to
 295 understand how the azimuthal distribution of the synthetic data affected its ability to
 296 constrain anisotropy.

298 2.4 Distinguishing the mechanism and orientation of anisotropy

299 For the first round of tests, we sought to understand how many shear wave splitting
 300 measurements, and in what combination (as described by the SKS number), are generally
 301 needed to uniquely constrain the *mechanism* for anisotropy. That is, we tested whether
 302 synthetic datasets could be shown to be consistent *only* with the correct starting model (e.g.,

1
2
3 303 Ppv, as opposed to other models listed in Table 1), and with *no other* candidate mechanism.
4
5 304 For this round of tests, we used the single crystal models in Table 1 as starting models,
6
7 305 each in several different orientations. The LPO model of Ppv was only used for the second
8
9 306 round of tests. We defined the starting model orientation via the rotation angle about the
10
11 307 [100] axis from the horizontal (note that Figure 2 only shows an example with a horizontal
12
13 308 [100] and [010] direction). We arbitrarily tested each single crystal model at three different
14
15 309 orientations based on the rotation angle about the [100] axis from the horizontal: 0°, 45°,
16
17 310 and 90°. For the LPO model of Ppv, we only test the original orientation for the starting
18
19 311 model and do not test a rotated version of the elastic tensor since this model is based on a
20
21 312 region in the Walker et al. (2011) with horizontal shear. In our initial round of tests, we
22
23 313 focused only on cases in which shear wave splitting observations of SKS, SKKS, and ScS
24
25 314 (for varying N, SKS number, and R values) were used to constrain the models; in later
26
27 315 tests, we explored scenarios in which reflection measurements were combined with shear
28
29 316 wave splitting data, in order to estimate the improvement obtained by combining different
30
31 317 data types.

32
33 318 We also carried out a series of tests whose goal was to constrain the *orientation* of
34
35 319 the elastic tensor for the case in which the mechanism for anisotropy is known (or
36
37 320 assumed). For this line of inquiry, we focused on Ppv as a test case; we did not test other
38
39 321 mechanisms in this part of the study. The choice to focus on Ppv was made for simplicity
40
41 322 and because Ppv is often invoked as the preferred mechanisms for anisotropy in D" (Creasy
42
43 323 et al., 2017; Ford et al., 2015; Ford and Long, 2015; Nowacki et al., 2010; Thomas et al.,
44
45 324 2011a; Wookey et al., 2005b). We consider both single-crystal Ppv tensors and elastic
46
47 325 tensors derived from texture modeling, as discussed above. As in our first series of tests,
48
49
50
51
52
53
54
55
56
57
58
59
60

1
2
3 326 we initially focus on synthetic datasets that only contain shear wave splitting observations,
4
5 327 and then examine cases that also include reflection measurements.
6
7

8 328 Lastly, in addition to the two major lines of inquiry we address in our modeling
9
10 329 (what kind of datasets are needed to constrain the *mechanism* and *orientation*) of lowermost
11
12 330 mantle anisotropy, we **performed** two practical tests using horizontal Ppv as a starting
13
14 331 model. First, we carried out a test of how many iterations (that is, values of M) are needed
15
16 332 for our forward algorithm to converge on an estimate of the probability of identifying
17
18 333 unique models. Second, we tested the addition of Gaussian noise to the shear wave splitting
19
20 334 predictions, in order to understand how well real, noisy datasets might perform. The results
21
22 335 of these practical tests are described below. **While seismic data can deviate from a Gaussian**
23
24 336 **distribution (Groos and Ritter, 2009), we only consider Gaussian distributed noise here**
25
26 337 **since in an ideal case, seismic noise is Gaussian distributed (Bendat and Piersol, 2011).**
27
28
29
30
31 338

32 339 **3. Results**

33 340 3.1 Illustrative examples: Model runs for a ppv starting model

34
35 341 To illustrate the process **and results** of our modeling, we discuss **here** the results
36
37 342 from a test that attempts to constrain the *starting model*, as well as one iteration of a test
38
39 343 that attempts to constrain the *orientation*. In both cases, we use synthetic shear wave
40
41 344 **splitting** data only. For these examples, as in all of our tests, we follow the **five** steps of our
42
43 345 method outlined above (**Figure 4**): (1) choose a starting model and orientation, (2) **choose**
44
45 346 **the number of observations and the SKS number to randomly generate a distribution of**
46
47 347 **raypaths**, (3) calculate the predicted **fast polarization directions (of SKS, SKKS, and ScS)**
48
49 348 **and reflection polarities (for SdS and PdP) for the synthetic dataset for the chosen starting**
50
51
52
53
54
55
56
57
58
59
60

1
2
3 349 model, (4) conduct a forward modeling search over all possible orientations for all possible
4
5 350 candidate models to eliminate all models/orientations that do not fit the “observations”
6
7
8 351 using a misfit cutoff. Then, if all other models and orientations can be eliminated by
9
10 352 applying the misfit cutoff, this set of synthetic raypaths are able to uniquely constrain the
11
12 353 starting model and designated as “*uniquely constrained*.” The fifth step would be repeating
13
14
15 354 this process M number of times but for this illustrative example, $M = 1$.

16
17 355 Our illustrative example is shown in Figure 5. For this example, we chose a starting
18
19 356 model of non-rotated Ppv (in this case, the [100] and [010] crystallographic axes are
20
21 357 parallel to the CMB) (Figure 5a). In all of our single-crystal elasticity tests, we do not
22
23 358 assume a dominant slip system; rather, we invoke a starting orientation in the geographic
24
25 359 reference frame identified by the angle of the mineralogical axes. This particular example
26
27
28 360 involves 9 splitting observations, 6 of which are SK(K)S (that is, an SKS number of 2/3).
29
30
31 361 The randomly generated azimuthal distribution of these chosen phases is shown in Figure
32
33 362 5b. The predicted fast polarization directions for our chosen model and ray configuration,
34
35 363 plotted in a ray-centered reference frame, are shown in Figure 5c. A search over all possible
36
37 364 candidate models and orientations (rotating every 5°) shows that there is no other model,
38
39
40 365 other than the correct starting model (Ppv), that can match each of the synthetic fast
41
42 366 splitting directions to within 20° (our pre-defined misfit cutoff). Put another way, for every
43
44 367 possible combination of starting model and orientation (other than the correct, known
45
46 368 starting model), at least one predicted fast splitting orientation differed from that in the
47
48 369 dataset by more than the 20° misfit cutoff. Since this particular configuration of
49
50
51 370 observations could uniquely identify the starting model and no other models, it is
52
53
54 371 designated “*uniquely constrained*.”
55
56
57
58
59
60

1
2
3 372 This particular example illustrates a single iteration ($M = 1$) of our testing, but the
4
5 373 power of our approach lies in repeating this a large number of times to understand what
6
7 374 percentage of randomly generated synthetic datasets have the ability to uniquely constrain
8
9 375 the starting model. In order to understand how many iterations are needed to converge on
10
11 376 an estimate of this probability, we conducted an “iteration test” for our horizontal Ppv
12
13 377 starting model, as shown in Figure 6. For this test, we used 9 shear wave splitting
14
15 378 measurements ($N = 9$) and an SKS number of $2/3$, as in the example shown in Figure 5,
16
17 379 and ran a large number of iterations ($M = 50,000$), each involving a new, random
18
19 380 distribution of propagation azimuths. After each successive iteration, we calculated the
20
21 381 percentage (of M iterations) for which the synthetic dataset was able to *uniquely constrain*
22
23 382 the starting model, as shown in Figure 6. For this starting model, after a large number of
24
25 383 iterations, we found that 41% of all iterations could uniquely constrain the starting model,
26
27 384 while for the other 59% of the raypath configurations, there was another model/orientation
28
29 385 that could *simulate* the synthetic data. Our running estimate of how likely a dataset with 9
30
31 386 splitting observations (6 SK(K)S, 3 ScS) converges on an average value of 41% after
32
33 387 approximately 1,000 iterations (Figure 5). Based on this iteration test, we have chosen to
34
35 388 run each of our numerical experiments for $M = 5,000$ iterations, balancing computational
36
37 389 cost and the need for our estimates to converge.

390 Next, to illustrate our process for testing whether synthetic data can identify a
391 unique starting *orientation*, we show in Figure 6 two examples of searching for the correct
392 starting orientation for the same horizontal Ppv starting model as in Figure 4. For this
393 example, we chose two different raypath configurations, one with $N = 8$ observations (5
394 SKS+SKKS and 3 ScS; Figure 7a) and one with $N = 4$ (3 SKS+SKKS and 1 ScS; Figure

1
2
3 395 7b). We assume that the mechanism for anisotropy is known to be Ppv and that the elastic
4
5 396 constants are known, and search over all possible orientations to test whether there are
6
7 397 additional configurations (other than the known starting orientation) that can reproduce the
8
9
10 398 synthetic observations.

11
12 399 Figures 7a and 7b show all possible orientations that satisfy this suitability criterion
13
14 400 for each of our two examples ($N = 8$ and $N = 4$, respectively), with each orientation color-
15
16
17 401 coded by its calculated misfit value (Equation 1). Following Ford et al. (2015), we search
18
19 402 for local minima of misfit within the 3-D rotation space. For our $N = 8$ case (Figure 7a),
20
21 403 the set of 8 measurements could uniquely identify the starting orientation, and would be
22
23
24 404 designated as “uniquely constrained.” However, for our $N = 4$ case (Figure 7b), we
25
26 405 identified two other possible orientations (that is, the known correct starting orientation,
27
28 406 plus two others). Therefore, for this particular raypath configuration, the solution is
29
30
31 407 designated “not uniquely constrained.” We note, however, that the orientation with the
32
33 408 lowest misfit value (magenta dot in Figure 7b) is, in fact, the correct starting orientation.

34
35 409 Finally, we illustrate an example calculation that includes Gaussian noise in the
36
37
38 410 synthetic observations (Figure 7c). This test relies on the same horizontal Ppv starting
39
40 411 model, and uses the same raypath configuration ($N = 4$) as the test shown in Figure 7b. The
41
42 412 only difference is that when the predicted shear wave splitting fast directions are calculated
43
44
45 413 based on the starting model and raypath distribution, we add Gaussian noise to the fast
46
47 414 splitting direction “observations,” with a maximum error excursion of 20° and a standard
48
49 415 deviation of 9° . Figure 7c reveals that the case with Gaussian noise produced the same two
50
51 416 possible sets orientations as fitting the data, but now the solution with the minimum misfit
52
53
54 417 is not associated with the correct solution.

1
2
3 418
45 419 3.2 Results: Constraining the anisotropy mechanism
6

7
8 420 Building on the illustrative examples discussed in section 3.1, we now explore the
9
10 421 results of a large number of simulations with different starting models and raypath
11
12 422 configurations. We first address the question of what kind of datasets are needed to
13
14 423 distinguish among the various models listed in Figures 2 and 3. For this suite of numerical
15
16 424 experiments, we examined a variety of starting models and orientations, as well as a variety
17
18 425 of raypath configurations (as defined by the number of splitting measurements, the SKS
19
20 426 number, and the angular dispersion of the raypath azimuths). The results of these
21
22 427 experiments are shown in Figure 8. We first examine those model runs that only included
23
24 428 shear wave splitting data, shown in the nine panels of Figure 8a.
25
26
27

28 429 We initially focus on the mechanism and orientation of the starting model (Figure
29
30 430 8a, left panels), and explore how the probability of uniquely constraining the mechanism
31
32 431 varies as a function of the number of measurements. For each of the models considered,
33
34 432 the probability of identifying the unique starting model increases with the number of
35
36 433 measurements, as expected, typically with a sharp increase in the probability for N values
37
38 434 between ~6-9. In all cases, approximately 9 measurements are needed in order to have a
39
40 435 ~50% chance of constraining the starting model, while a high number of splitting
41
42 436 measurements ($N \approx 15$) is needed for the probability to reach ~90%. (For comparison, the
43
44 437 datasets of Ford et al. (2015) and Creasy et al. (2017) contained between 4-8 splitting
45
46 438 measurements.) The starting model with the highest success rate at constraining the
47
48 439 mechanism is Br, as opposed to Fp and Ppv.
49
50
51
52
53
54
55
56
57
58
59
60

1
2
3 440 The probability of constraining the starting mechanism depends on the orientation
4
5
6 441 of the starting model; as shown in Figure 8a, we tested orientations with a horizontal [100]
7
8 442 crystallographic axis, 45° rotated about the [100], and 90° rotated about the [100] axis.
9
10 443 Interestingly, for Ppv it is easier to uniquely constrain the starting model in the 90° case;
11
12 444 in contrast, for Br the chances are highest for **the horizontal case**, and for Fp the chances
13
14 445 are substantially higher for **the tilted case**. The reason for this **result** for Ppv can be
15
16 446 discerned by examining the predicted splitting patterns in Figure 2. For **the horizontal case**,
17
18 447 predicted fast splitting directions for ScS do not vary with azimuth; however, if the Ppv
19
20 448 tensor is rotated by 90° about the [100] axis, there is significant variation in fast directions
21
22 449 with azimuth. With greater variability in the predicted fast polarization directions (**lower**
23
24 450 **angular dispersion**), there is a higher probability of constraining that model for a given
25
26 451 number of ScS observations. A similar principle is at work for Fp: ScS fast directions do
27
28 452 not vary with azimuth for either horizontally or vertically aligned Fp, but **in the tilted case**,
29
30 453 variability is present. **Generally, the anisotropy scenarios that yield higher chances of**
31
32 454 **uniquely constraining the starting model have lower mean angular dispersion values of the**
33
34 455 **predicted fast-axis directions (Supplementary Figure S2). Models that have little variation**
35
36 456 **in fast-axis directions with azimuth, such as non-rotated Fp, are more difficult to uniquely**
37
38 457 **constrain (Figure S2c and Figure 8a).**

39
40 458 We also examined how the balance between SKS+SKKS vs. ScS phases in the
41
42 459 synthetic dataset affected the ability of the **synthetic** “observations” to uniquely constrain
43
44 460 the starting model (Figure 8a, middle panels). For these experiments, we varied the SKS
45
46 461 number from 0 (all ScS measurements) to 1 (all SKS+SKKS measurements) for a fixed
47
48 462 value of $N = 9$. For very high or low values of SKS number we find a low probability of
49
50
51
52
53
54
55
56
57
58
59
60

1
2
3 463 uniquely constraining the starting model with substantially higher probabilities for
4
5 464 intermediate SKS numbers. The optimal ratio of SK(K)S phases to total measurements
6
7 465 differs slightly for different starting models, but in general an SKS number between 0.5
8
9 466 and 0.8 maximizes the chances of constraining the anisotropic mechanism. In all cases, a
10
11 467 combination of ScS and SK(K)S shear wave splitting observations, instead of splitting
12
13 468 measurements for just one phase type, will drastically improve the probability of
14
15 469 constraining the starting model.
16
17
18

19 470 Additionally, we explored the importance of how the angular distribution of the
20
21 471 synthetic raypaths affected the ability to constrain the starting model, finding only a weak
22
23 472 effect (Figure 8a, right panels). As expected, datasets with a wide angular distribution (R
24
25 473 < 0.2) have the largest probability of uniquely constraining the starting model in all cases.
26
27
28 474 At very large values of angular dispersion ($R > 0.8$), for which the raypaths are clustered
29
30 475 over a narrow range of azimuths, the splitting “observations” are sampling similar parts of
31
32 476 the elastic tensor. Because of this, datasets that are tightly clustered in azimuth cannot
33
34 477 capture the symmetry of the tensor and cannot distinguish among different candidate
35
36 478 mechanisms for anisotropy. For intermediate values of R , the dependence on R is not
37
38 479 strong.
39
40
41

42 480 Finally, we explored the value of combining shear wave splitting and reflection
43
44 481 polarity measurements when trying to uniquely constrain an anisotropic model. Figure 8b
45
46 482 shows the results of adding a single reflection polarity measurement (that is, a measurement
47
48 483 of PdP and SdS polarities for a single raypath) to a dataset of shear wave splitting
49
50 484 measurements. For this test, we considered a smaller number (four) of potential candidate
51
52 485 models (as shown in Figure 3), so the probabilities of uniquely constraining the anisotropy
53
54
55
56
57
58
59
60

1
2
3 486 mechanism are generally higher than in our other tests. For this test, we chose a raypath
4
5 487 configuration involving an SKS number of 0.67 and varied the number of shear wave
6
7 488 splitting measurements from 0 to 15. We used a starting model A in Figure 3 (anisotropy
8
9 due to Ppv), and tested configurations that involved both shear wave splitting
10 489 measurements and one additional set of reflection polarity measurements (both PdP and
11
12 490 SdS) at a single azimuth. This test (Figure 8b) demonstrates that despite the fact that
13
14 491 reflectivity measurements provide only binary information (positive or negative polarities),
15
16 492 the incorporation of a different data type into the test increases the probability of uniquely
17
18 493 constraining the starting model. In some cases, this increase is substantial; specifically, for
19
20 494 datasets containing between 4 and 8 shear wave splitting measurements. The addition of
21
22 495 reflection polarity data can increase the probability of constraining the starting model by
23
24 496 ~10-18% (right panel of Figure 8b).
25
26
27
28
29
30
31
32

33 499 3.3 Results: Constraining the anisotropy orientation

34
35 500 The tests shown in Figure 8 illustrate the ability of shear wave splitting and
36
37 501 reflection polarity data to constrain the anisotropic mechanism if the algorithm is allowed
38
39 502 to consider a range of possible models. We now turn our attention to tests in which we
40
41 503 assume that the mechanism that creates the anisotropy, as well as the elastic constants
42
43 504 associated with that mechanism, are known, but the orientation of the elastic tensor is not
44
45 505 known. In general, this is an easier problem than uniquely constraining the starting model,
46
47 506 as the observations need not distinguish among different candidate elastic tensors, only
48
49 507 among different possible orientations. In practical terms, this type of modeling exercise
50
51 508 would be suitable for datasets that sample a region of the lowermost mantle whose
52
53
54
55
56
57
58
59
60

1
2
3 509 mineralogy and temperature conditions can be constrained using independent observations
4
5 510 or models (for example, seismic velocities in combination with mineral physics
6
7
8 511 constraints).

9
10 512 For this set of tests, we first consider single-crystal Ppv in three different
11
12 513 configurations: 1) [100] and [010] axes oriented in the horizontal plane, 2) a 90° rotation
13
14 514 about the [100] axis, and 3) randomly chosen orientations. For the third configuration, we
15
16 515 randomly identified nine different, unique starting orientations. These randomly generated
17
18 516 orientations were used for each of the ~5,000 iterations in this scenario. As with the tests
19
20
21 517 discussed in section 3.2, we tested a variety of raypath configurations with a range of N
22
23
24 518 (number of measurements), SKS number, and examined how our results varied with the
25
26 519 angular dispersion characteristics of the synthetic raypaths. The results of our single-crystal
27
28 520 Ppv tests are shown in the top row of Figure 9. The results for our collection of nine random
29
30 521 starting orientations are shown in detail in Supplementary Figure S3.

31
32
33 522 As expected, our tests demonstrate that uniquely constraining the orientation of the
34
35 523 starting model is much easier and requires fewer measurements than uniquely constraining
36
37 524 the starting model/mechanism (Figure 7). In general, a ~50% probability of correctly
38
39 525 retrieving the anisotropy is achieved with ~6-9 splitting measurements (top left panel of
40
41
42 526 Figure 9a). The orientation of the starting model does affect the likelihood of uniquely
43
44 527 identifying the anisotropy orientation. With our randomly generated starting orientations,
45
46 528 the probability of constraining the starting orientation varies (Figure S3), but on average
47
48 529 randomly oriented starting models do slightly worse compared to the results shown in
49
50 530 Figure 9. For six measurements, the randomly orientated models on average find the correct
51
52 531 orientation in 65% of all simulations, compared to Figure 9, where a non-rotated and Ppv
53
54
55
56
57
58
59
60

1
2
3 | 532 rotated by 90° can constrain on average 75% of the simulations. As with our previous tests,
4
5 | 533 it is clear that a mixture of SK(K)S and ScS shear wave splitting measurements provide
6
7 | 534 the highest likelihood of constraining the starting orientation, although the optimal mix of
8
9 | 535 ScS and SK(K)S depends on the starting model orientation. Our tests confirm that datasets
10
11 | 536 that contain only ScS measurements (that is, SKS number of zero) cannot constrain the
12
13 | 537 azimuth of the Ppv elastic tensor if its [100] axis is horizontal, due to the lack of variability
14
15 | 538 in predicted fast polarization direction (Figure 2). The dependence of our results on angular
16
17 | 539 dispersion of the propagation azimuths (right panels of Figure 9a) are similar to those for
18
19 | 540 the case in which we attempted to retrieve the starting model; in general, a wide distribution
20
21 | 541 of azimuths will increase the probability of uniquely constraining the orientation of Ppv,
22
23 | 542 while datasets whose propagation azimuths are tightly clustered are less ideal. The same is
24
25 | 543 generally true for the random starting models, despite some small excursions from the
26
27 | 544 overall trend (Figure S3). These small excursions or “bumps” in the curves are artifacts,
28
29 | 545 and are related to stochastic variations in the distribution of the predicted fast splitting
30
31 | 546 directions for different models.
32
33
34
35
36
37

38 | 547 Next, we considered elasticity models that explicitly take into account texture
39
40 | 548 development in a polycrystalline aggregate, in addition to the single-crystal elastic tensors
41
42 | 549 that are the main focus of our study. While there are many uncertainties in texture models
43
44 | 550 for Ppv at lowermost mantle conditions, these models may be more representative of a
45
46 | 551 realistic texture of aligned Ppv mineral grains. We only considered one case, invoking
47
48 | 552 dominant slip on the (010) plane. Somewhat surprisingly, we found that for modeled Ppv
49
50 | 553 LPO, there is a much lower probability of constraining the orientation of the elastic tensor
51
52 | 554 than for test cases that used a single crystal elastic tensor (Figure 8a). We investigated
53
54
55
56
57
58
59
60

555 possible reasons for this, and found that in contrast to the single-crystal models, for the
556 textured Ppv model it is fairly common for the algorithm to identify what we term as
557 “unstable” solutions, which are illustrated in Figure S4. In this situation, a certain
558 orientation might fit the observations, but adjacent orientations (in which the elastic tensor
559 is rotated by 5°) do not. This is in contrast to the behavior of single-crystal elastic models
560 (Figure 2), in which the best-fitting orientations are adjacent to other solutions that also fit
561 the data (in other words, the misfit values vary smoothly as a function of rotation angles of
562 the candidate tensors). In addition, the presence of unstable solutions is highly dependent
563 on our use of the misfit criterion of 20°. Figure S4 shows results for a range of misfit cutoff
564 values, and demonstrates that these unstable solutions disappear with the application of
565 more conservative misfit criteria.

566 We define a “stable” solution as one in which, if the elastic tensor is rotated slightly
567 (~5° in any direction), the rotated elastic tensor would still yield an acceptable fit to the
568 synthetic data. In contrast, an “unstable” solution is one that has no adjacent orientations
569 that yield an acceptable fit to the data. For the case of the textured Ppv model, the algorithm
570 generally identifies many “unstable” orientations (Figure 9); again, this is in contrast to the
571 generally “stable” orientations identified for single-crystal Ppv (Figure 7). In order to
572 illustrate the effects of these unstable solutions, we applied a sensitivity cutoff to our
573 textured Ppv simulations (Figure 8a, second row) to illustrate the effects of removing all
574 unstable solutions. If we consider only stable solutions, the probability of uniquely
575 constraining the starting orientation increases by 20% on average (Figure 9a).

576 In order to identify the starting orientation of the Ppv LPO, we found that a mixture
577 of SK(K)S and ScS shear wave splitting measurements again provide the highest likelihood

1
2
3 578 of constraining the orientation (Figure 8a: bottom, middle panel). There is a clear
4
5 579 dependence on angular dispersion (Figure 9a: bottom, right panel). Specifically, with low
6
7
8 580 values of R (0-0.1) and middle values of R (0.5-0.7), there is a higher probability of
9
10 581 constraining the orientation, while there is a decrease in probability between R = 0.1 and
11
12 582 R = 0.4. In all other cases and starting models, we have not observed this pattern of
13
14 583 dependence with R. While there is no explanation for this pattern, large values of R (0.8-
15
16 584 1.0) resulting in low probabilities of finding the starting orientation is consistent with all
17
18
19 585 other tests.

20
21 586 Returning to our consideration of single-crystal Ppv models, and as in section 3.2,
22
23 587 we considered the effect of adding a reflection measurement to shear wave splitting
24
25 588 observations to constrain the orientation of the single-crystal Ppv starting model (Figure
26
27 589 9b). For this test, we used a starting model that invokes an isotropic pvp layer over an
28
29 590 anisotropic pvp layer with dominant [100](010) slip (Model A in Figure 3). As in the
30
31 591 previous test, we find that just adding one observation of reflection polarity measurements
32
33 592 improves the probability of constraining the starting orientation (Figure 9b), although the
34
35 593 improvement was somewhat less dramatic. Again as with the previous tests, the relative
36
37 594 improvement is greatest for datasets with number of measurements N roughly between 5
38
39 595 and 9.

40
41 596 Finally, in a test analogous to the Gaussian noise test discussed in section 3.1 and
42
43 597 illustrated in Figure 7c, we considered a single-crystal Ppv test in which we tried to retrieve
44
45 598 the correct starting orientation using synthetic observations that included random, Gaussian
46
47 599 distributed errors on the fast polarization predictions (Figure 10). We found that adding
48
49 600 Gaussian noise to the fast polarization directions, normally distributed between -20° and
50
51
52
53
54
55
56
57
58
59
60

1
2
3 601 20° with a mean of 0° and standard deviation of 9°, does not significantly hinder the
4
5 602 probability of constraining the starting model's orientation (Figure 10a). However, this test
6
7 603 allowed us to explore the distinction between *uniquely* constraining the starting model's
8
9 604 orientation and identifying a model with a *minimum* misfit value that corresponds to the
10
11 605 correct starting orientation. For the error-free synthetic datasets, the minimum misfit value
12
13 606 always corresponds to the correct orientation, even for cases in which other orientations
14
15 607 are allowed by the data. For cases in which Gaussian error is incorporated to the synthetic
16
17 608 dataset; however, it is possible for the orientation with the minimum misfit value to be
18
19 609 different from the correct solution. This observation led us to carry out a test (Figure 10b)
20
21 610 in which rather than attempting to *uniquely* constrain the correct starting orientation, we
22
23 611 tested whether the best-fitting orientation (that is, the candidate orientation with the
24
25 612 minimum misfit value) actually corresponded to the correct starting orientation. We further
26
27 613 tested whether the best-fitting solution in terms of misfit was oriented within 10°-20° of
28
29 614 the known, correct starting orientation. Encouragingly, we found that the probability that
30
31 615 the minimum misfit solution was within 20° of the correct orientation exceeded 50% for
32
33 616 datasets with a relatively small number of shear wave splitting measurements ($N \approx 4$).
34
35
36
37
38
39
40
41

42 618 **4. Discussion**

43
44 619 Understanding the scope of information about lowermost mantle anisotropy
45
46 620 contained in body wave datasets (specifically, shear wave splitting and reflection polarity
47
48 621 observations) is crucial for our ability to relate anisotropy observations to flow at the base
49
50 622 of the mantle. While the mechanism(s) of lowermost mantle anisotropy remain imperfectly
51
52 623 known, the results presented in this paper reveal observational strategies that can maximize
53
54
55
56
57
58
59
60

1
2
3 624 the probability of constraining the mechanism and/or orientation, regardless of the actual
4
5 625 anisotropic geometries present. This work shows that a diversity of methods (shear wave
6
7
8 626 splitting measurements on a variety of seismic phases, plus reflection polarity data) should
9
10 627 be applied in individual regions of the lowermost mantle, and the simultaneous
11
12 628 interpretation of multiple types of observations significantly increases the chances of
13
14
15 629 placing strong constraints on anisotropic geometry.

16
17 630 Specifically, this work demonstrates that because different seismic phases (ScS,
18
19 631 SKS, SKKS, PdP, SdS) propagate through (or reflect off) the D" region at different angles
20
21 632 from the horizontal, a combination of these phases is particularly powerful and has an
22
23 633 increased ability to constrain anisotropy than datasets that have good azimuthal coverage,
24
25
26 634 but only include one type of measurement. While datasets with wide azimuthal coverage
27
28 635 are useful, the application of a single measurement methodology (e.g., ScS shear wave
29
30
31 636 splitting) has only limited utility. For example, if only ScS (or SKS) splitting measurements
32
33 637 are used to probe an anisotropic model of a horizontal, single crystal post-perovskite, then
34
35 638 post-perovskite can be distinguished from other scenarios less than 10% of the time, if 9
36
37 639 unique measurements are used (Figure 8a and 9a). However, if SK(K)S phases and/or
38
39
40 640 reflection polarities are incorporated into the analysis, then the dataset may be able to
41
42 641 distinguish between the two possible mechanisms nearly 40% of the time (Figure 8a). In
43
44 642 all cases of varying starting models and orientations, a combination of different types of
45
46 643 data increases the probability of constraining the starting model by 10% to 60%. This
47
48 644 pattern also generally holds true for finding the orientation of the Ppv elastic tensor. A
49
50
51 645 diversity of data can improve the ability to constrain the orientation of Ppv anisotropy
52
53
54 646 anywhere from 10% to 50% for 6 unique measurements. Interestingly, we observed an
55
56
57
58
59
60

1
2
3 647 exception to this (Figure 9a) for Ppv oriented at an azimuth of 90°, where only ScS splitting
4
5 648 data (SKS number of 0) had the best chance to constrain the starting orientation.
6
7

8 649 Ideally, body wave datasets that probe seismic anisotropy in the lowermost mantle
9
10 650 should combine both multiple data types and wide azimuthal coverage to maximize the
11
12 651 probability that the anisotropic geometry can be tightly constrained. Figure 11 illustrates
13
14 652 regions in the mantle in which all of the body wave measurement methods could potentially
15
16 653 be applied simultaneously. This map was generated by considering the actual distribution
17
18 654 of high-magnitude ($M > 6.5$) seismicity on Earth, in combination with a database of long-
19
20 655 running broadband seismic stations beneath which the upper mantle anisotropy pattern has
21
22 656 been shown to be simple enough to correct for (Lynner and Long, 2013, 2014b). While
23
24 657 there are many regions of D'' with limited raypath coverage for the types of data considered
25
26 658 in this study, we find that North America, the Arctic, northwestern Pacific, and Australia
27
28 659 are regions that represent ideal targets to collect a diverse set of observations to further
29
30 660 constrain D'' anisotropy.
31
32
33
34

35 661 Our results indicate that a relatively large number of shear wave splitting
36
37 662 measurements (approximately 9 or more for most cases in Figure 8a) are needed to have at
38
39 663 least a 40% to 60% chance of uniquely identifying the starting model. Typical
40
41 664 observational datasets include approximately four to eight shear wave splitting
42
43 665 measurements over unique azimuths in the lowermost mantle (Table 3) (e.g., Ford et al.,
44
45 666 2015; Creasy et al., 2017). The synthetic models presented in this paper help to provide
46
47 667 context for why these studies have not been able to uniquely constrain a particular
48
49 668 mechanism or orientation for anisotropy (e.g. Ford et al., 2015, Creasy et al., 2017). For
50
51 669 example, each of these studies (Table 3) had relatively high angular dispersion values for
52
53
54
55
56
57
58
59
60

1
2
3 670 their range of predicted fast splitting directions (greater than 0.4 in all cases). As discussed
4
5 671 in section 3.2, data sets with lower angular dispersion values are generally more successful
6
7
8 672 at constraining a unique elastic tensor. Therefore, even though many of the studies listed
9
10 673 in Table 3 used diverse data types with combinations of SKS, SKKS, and ScS, they
11
12 674 struggled to identify a uniquely constrained anisotropy mechanism or orientation. The
13
14
15 675 studies that used one type of observation (Nowacki et al., 2010; Thomas et al., 2011) did
16
17 676 not consider all possible elastic tensors and orientations that we tested here, so we cannot
18
19 677 directly compare them with the results of our synthetic tests. On a more optimistic note,
20
21
22 678 our work shows that if the mechanisms for anisotropy (and the associated elastic tensors)
23
24 679 can be reliably assumed, there is generally a higher chance of identifying the correct
25
26 680 orientation (and therefore of inferring the correct mantle flow geometry). With only 9
27
28 681 measurements, there is a 40% to 80% chance of uniquely constraining the orientation of
29
30
31 682 post-perovskite (Figure 9a), an improvement from the chance of uniquely identifying the
32
33 683 elastic tensor itself (a 40%-60% chance).

34
35 684 Our tests that include Gaussian error on the predicted fast splitting directions
36
37 685 (Figure 10b) demonstrate that it does not significantly affect the probability of constraining
38
39
40 686 the model, as compared to noise-free synthetic data. When including Gaussian error, we
41
42 687 found that as few as four shear wave splitting measurements can identify the correct
43
44 688 orientation within 20° more than 50% of the time. Datasets of this size can likely be
45
46
47 689 reasonably achieved in many regions of the lowermost mantle, based on the distribution of
48
49 690 available raypaths (Figure 11). This finding may help with the interpretation of modeling
50
51
52 691 results for real splitting datasets, such as those considered by Ford et al. (2015) and Creasy

1
2
3 692 et al. (2017), for which multiple possible anisotropic orientations were identified, but
4
5 693 particular orientations had significantly lower misfit values than others.
6
7

8 694 Our synthetic modeling results also shed light on potential complications in
9
10 695 interpretation caused by the different symmetry classes of some of the candidate elasticity
11
12 696 scenarios that have been proposed to explain lowermost mantle anisotropy. To effectively
13
14 697 differentiate these scenarios using shear wave splitting data alone, it is crucial for splitting
15
16 698 datasets to probe the symmetry of the mineral such that no other elastic tensor simulates
17
18 699 that pattern for a similar range of propagation directions. Of the candidate scenarios we
19
20 700 tested in this study, Fp has the highest (cubic) symmetry with only 3 unique constants in
21
22 701 the elastic tensor. SPO models have the next highest symmetry, since tubule and oblate
23
24 702 SPO models are hexagonal (transversely isotropic) with 5 unique elastic constants. Ppv and
25
26 703 Br are both orthorhombic, with the same order of symmetry and only 9 unique elastic
27
28 704 constants. In more complicated models, like LPO calculations of single crystals, the
29
30 705 symmetry is much lower than its single crystal counterpart with 21 unique elastic constants.
31
32

33 706 We caution that our synthetic tests must be interpreted in light of the still-
34
35 707 considerable limitations in our understanding of the elasticity of anisotropic materials at
36
37 708 lowermost mantle conditions. We have focused mainly on single-crystal elastic tensors,
38
39 709 derived mainly from ab initio simulations, as a reasonable starting point in this study;
40
41 710 however, predictions of single-crystal elasticity are likely imperfect and do not take into
42
43 711 account effects such as variation in composition. Furthermore, single-crystal elasticity is
44
45 712 an imperfect proxy for the likely anisotropic geometry of polycrystalline aggregates,
46
47 713 particularly for minerals with high symmetry such as Fp (e.g., Yamazaki and Karato,
48
49 714 2002). The further consideration of elasticity models that explicitly take into account
50
51
52
53
54
55
56
57
58
59
60

1
2
3 715 texture development will be an important step, although texture models include a number
4
5 716 of poorly known parameters (such as activation energies for different slip systems) and
6
7 717 consensus on the dominant slip systems in different lowermost mantle minerals remains
8
9 718 elusive (e.g., Nowacki et al., 2011).

10
11
12 719 Another limitation of the work proposed here is that it is carried out in the context
13
14 720 of ray theoretical predictions, assuming infinite frequency, rather than considering the full
15
16 721 characteristics of the waveform at finite frequencies. With improvements on both
17
18 722 observational and modeling techniques that model the full waveform (e.g., Kawai and
19
20 723 Geller, 2010, Nowacki and Wookey, 2016, Parisi et al., 2018), the interpretation of seismic
21
22 724 anisotropy observations can very likely be improved. In particular, future work must
23
24 725 investigate how the measurement techniques used influence the interpretation of finite
25
26 726 frequency waveform effects and to what extent ray theoretical predictions are a useful
27
28 727 approximation. Despite these limitations, we expect that future work that predicts body
29
30 728 wave observations in the presence of lowermost mantle anisotropy in a finite-frequency
31
32 729 framework will likely find similar results: a diversity of seismic phases and measurement
33
34 730 yields the best probability of capturing the symmetry, orientation, and properties of an
35
36 731 elastic tensor. While this study is limited to a specific set of currently-available elastic
37
38 732 tensors from the mineral physics literature, our overall findings should be generally
39
40 733 applicable and adaptable to future improvements of our knowledge of lowermost mantle
41
42 734 elasticity.

43
44
45
46
47
48
49 735

50
51 736 **5. Summary**
52
53
54
55
56
57
58
59
60

1
2
3 737 To summarize, the complete characterization and interpretation of seismic
4
5 738 anisotropy at the base of the mantle would have profound effects on our understanding of
6
7
8 739 lower mantle dynamics, potentially yielding insights into the pattern of mantle flow. Many
9
10 740 recent studies have pointed to the difficulty of distinguishing different models of lowermost
11
12 741 mantle anisotropy with body wave observations, given challenges with data coverage and
13
14 742 uncertainties in the mechanism for anisotropy and the relationships between deformation
15
16 743 and the resulting anisotropy at lower mantle conditions. In this study, we conducted a series
17
18
19 744 of Monte Carlo simulations to determine what kinds of body wave datasets (shear wave
20
21 745 splitting and reflection polarities) are required to constrain D" anisotropy. We tested
22
23 746 various starting models, orientations, and methods and identified what kind of observations
24
25
26 747 are needed to distinguish these models. The modeling approach and philosophy in this
27
28 748 study is applicable to a wide range of elasticity models, and can be extended as our
29
30 749 knowledge of the physical properties of the lowermost mantle increases. Our results show
31
32
33 750 that a diversity of observational techniques, including different types of seismic phases
34
35 751 propagating over a range of raypath directions, are necessary in order to maximize the
36
37
38 752 chances of constraining anisotropy at the base of the mantle. A combination of shear wave
39
40 753 splitting measurements and observations of PdP and SdS reflection polarities in the same
41
42 754 regions may be particularly powerful. We have further shown that if the mineralogy and/or
43
44 755 mechanism for anisotropy can be constrained from independent data, then the orientation
45
46 756 of the elastic tensor (and thus information about patterns of mantle flow) can likely be
47
48
49 757 retrieved from observational datasets that include a relatively modest number of
50
51 758 measurements.
52
53
54
55
56
57
58
59
60

759 **Tables**

760 Table 1

761 Summary of all elastic tensors used in the forward modeling. Columns show the type of
 762 tensor (single-crystal, LPO based on experimental data, SPO based on effective medium
 763 averaging, or LPO based on global flow and texture models), the phases and/or
 764 constituents, and the reference. For the single-crystal tensors, the pressure and temperature
 765 conditions used in the modeling are also indicated. ¹Elastic tensors used for tests to
 766 uniquely constrain the starting model. ²Elastic tensors used for tests to uniquely constrain
 767 the orientation.

Single Crystal Tensors

Geometry	Phase	Pressure (GPa)	Temperature (K)	References
Single Crystal	Br ¹	125	2500	<i>Wentzovitch et al.</i> [2006], <i>Wookey et al.</i> [2005a, 2005b]
		126	2800	
		136	4000	
	Ppv ^{1,2}	135	4000	<i>Stackhouse et al.</i> [2005]
	MgO ¹	135	3000	<i>Karki et al.</i> [1999]

Other Tensors

Geometry	Phase	Notes	References
Experimental LPO	MgO ¹	P = 0.3 GPa; T = 1473K	<i>Long et al.</i> [2006]
SPO ¹	0.003 vol. fraction melt	Oblate shape	<i>Walker and Wookey</i> [2012]
	0.003 vol. fraction melt	Tubule shape	
Calculated LPO ²	Ppv	TX2008-V1 model; dominant slip plane: (010), P = 125-136; T = 3000-4000 K	<i>Walker et al.</i> [2011]; Tensors based on <i>Stackhouse et al.</i> , [2005] and <i>Stackhouse and Brodholt</i> [2007]

768

769

770

771 Table 2

772 Models for the top (isotropic) and bottom (anisotropic) layers of each model described in
 773 Figure 3 for reflection polarity models. The dominant slip system assumed in each bottom
 774 layer is listed.

Model	Top Layer (isotropic)	Bottom Layer (anisotropic)	Slip System	References
A	Ppv	Ppv	[100](010)	<i>Walte et al. [2009]</i> <i>Wentzcovitch et al. [2006]</i>
B	Br	Ppv	[100](010)	<i>Walte et al. [2009]</i> <i>Wentzcovitch et al. [2006]</i>
C	Br	Br	[010](100)	<i>Stackhouse et al. [2005]</i> <i>Mainprice et al. [2008]</i>
D	Fp	Fp	[100](001)	<i>Karki et al. [1999]</i>

775

776

777 Table 3

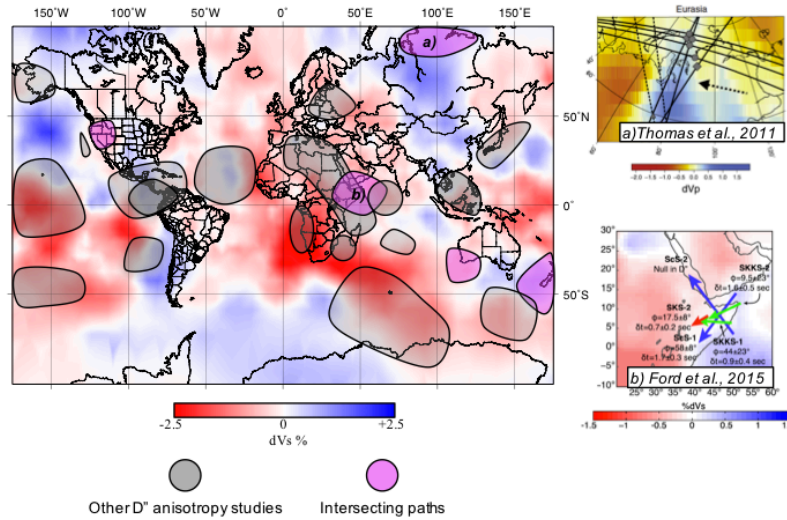
778 Summary of previous studies that have used crossing raypaths to study D'' anisotropy, as
 779 identified in Figure 1. The number of unique azimuths is given; each azimuth typically
 780 contains multiple observations (in practice, these observations are typically averaged for
 781 each set of raypaths). SKS number is calculated as defined in the text; for example,
 782 Nowacki et al. (2010) used only ScS phases, therefore the SKS number is 0. Angular
 783 dispersion (R) of the raypath azimuths is also calculated as described in the text.

References	Region	Number of Unique Azimuths	SKS Number	R
Creasy et al., 2017	New Zealand	8	0.75	0.7866
Creasy et al., 2017	SW Australia	4	0.5	0.4297
Ford et al., 2015	Afar Peninsula	5	0.6	0.8305
Thomas et al., 2011	Siberia + Caribbean	4	reflection polarities	0.5801
Nowacki et al., 2010	Caribbean	6	0	0.5734

784

1
2
3 **785 Figure Captions**
4

5
6 786 Figure 1. Summary map of previously published studies (which include shear wave
7
8 787 splitting measurements and reflection polarity observations) to constrain D" anisotropy,
9
10 788 updated and adapted from Nowacki et al. (2011). Highlighted areas (pink/gray) indicate
11
12 789 regions that have been probed for D" anisotropy with these methods. Regions in pink
13
14 790 indicate studies that used multiple techniques and/or intersecting ray paths, for which at
15
16 791 least two observations intersect in the same region with different propagation azimuths.
17
18 792 Two such studies are highlighted on the right. Panel (a) shows the raypaths (black lines)
19
20 793 beneath Siberia studied in the reflection polarity study of Thomas et al. (2011). CMB
21
22 794 bounce points are indicated with diamonds and circles, and the dotted arrow indicates paleo
23
24 795 subduction direction 100 Ma ago of the Kula **plate**. Background colors indicate P wave
25
26 796 velocity deviations at the base of the mantle from the model of Kárason and Hilst (2001).
27
28 797 Panel (b) shows a schematic diagram of shear wave splitting measurements of SKS (green),
29
30 798 SKKS (red) , and ScS (blue) phases beneath the Afar region of Africa (Ford et al., 2015).
31
32 799 Background colors show S wave velocity deviations at a depth of 250 km above core
33
34 800 mantle boundary from the GyPSuM tomography model (Simmons et al., 2010).
35
36
37
38
39
40
41
42
43
44
45
46
47
48
49
50
51
52
53
54
55
56
57
58
59
60



801

802

803

804

805

806

807

808

809

810

811

812

813

814

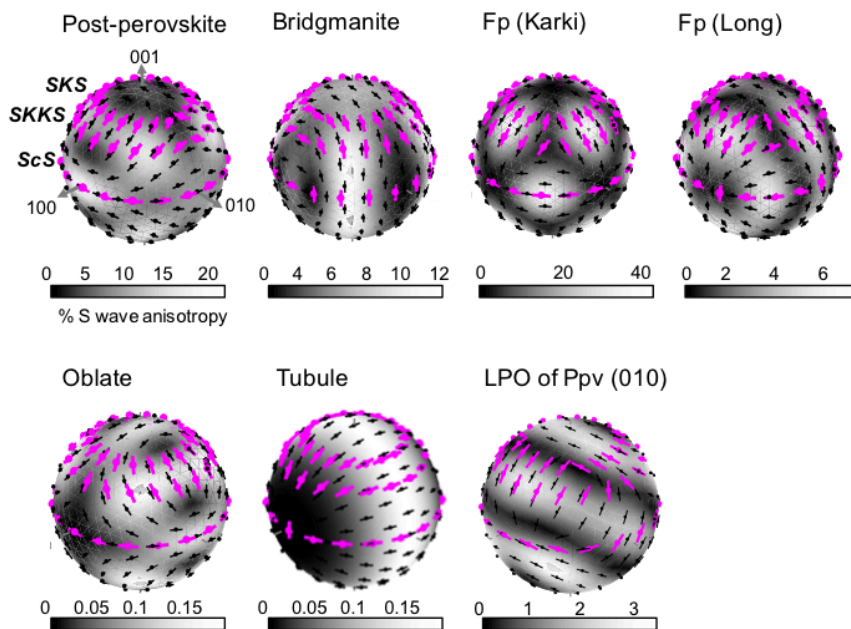
815

816

Figure 2. Elastic properties of models from Table 1 for D'' anisotropy tested in this study, as expressed in the predicted shear wave splitting behavior. Predicted shear wave splitting behavior is shown as a 3D spherical representation relative to geographic space, with the [100], [010], and [001] axes indicated in order to view the variation of splitting of SKS, SKKS, and ScS with azimuth. The anisotropy 3-D spheres show the directional dependence of seismic anisotropy (strength [gray color bar] and fast-axis directions [black bars]). For each model, the [100] and [010] axes are parallel to the CMB and oriented north and west, respectively. Black bars show predicted splitting over a range inclinations and azimuths, as computed using the MSAT toolkit (Walker and Wookey, 2012). Magenta bars illustrate the predicted fast polarization directions for the given starting models for a particular set of SKS, SKKS, and ScS raypaths every 20° (we actually use steps of 5° in the synthetic modeling, but the plotting is too dense to show) that are evenly distributed. Inclination angles used in the modeling are based on the average inclination angles for each phase through the D'' layer; we assume that ScS propagates nearly horizontally through the lowermost mantle, as described in the text. From left to right, we show elastic tensor models

817 for single-crystal Ppv (Stackhouse et al., 2005), single-crystal Br (Wentzcovitch et al.,
 818 2006), single-crystal Fp (Karki et al., 1999: Labeled as "Fp (Karki)"), experimentally-
 819 derived LPO of Fp (Long et al., 2006: Labeled as "Fp (Long)"), Oblate SPO (Walker and
 820 Wookey, 2012), Tubule SPO (Walker and Wookey, 2012), and the averaged, textured Ppv
 821 (Walker et al., 2011). Background colors are %S-wave anisotropy.

822



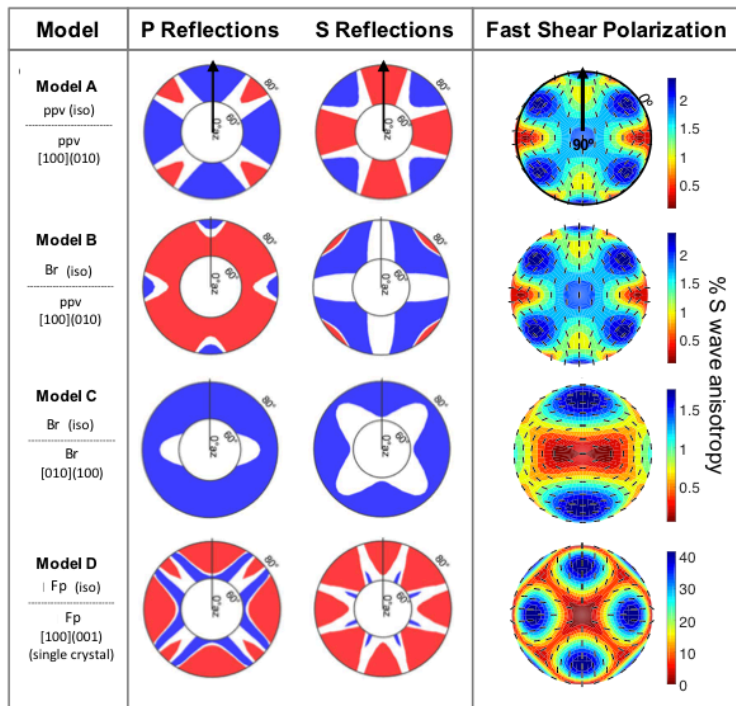
823

824

825 Figure 3. Predictions of reflection polarities for PdP and SdS waves for different
 826 D'' anisotropy models shown as an upper hemispherical projection since polarities depend
 827 on azimuth, not inclination as in Figure 2. Predictions are made as a function of azimuth
 828 and epicentral distance (from 60° to 80°). Azimuth is relative to the slip direction (indicated
 829 by the black arrow), which also corresponds to direction of lowermost mantle flow for a
 830 simple horizontal shear geometry. The first two columns show the reflection coefficients
 831 of P-P and SH-SH upon reflection off the D'' discontinuity, located 300 km above the core

832 mantle boundary in the model. Blue and red regions indicate positive and negative
 833 polarities, respectively. Models A, C, and D illustrate situations where there is an onset of
 834 anisotropy at the D" discontinuity while Model B invokes both a phase change (from Br to
 835 Ppv) and the onset of anisotropy. The last column illustrates the predicted S wave
 836 anisotropy (color bar) and predicted shear wave splitting fast directions (black bars) for the
 837 same models, plotted as a function of azimuth and inclination from the horizontal. Elastic
 838 tensors corresponding to these models are shown in Table 2.

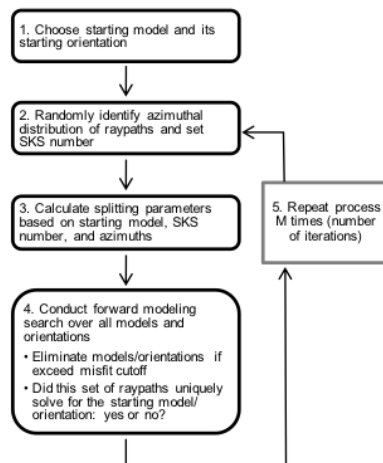
839



840

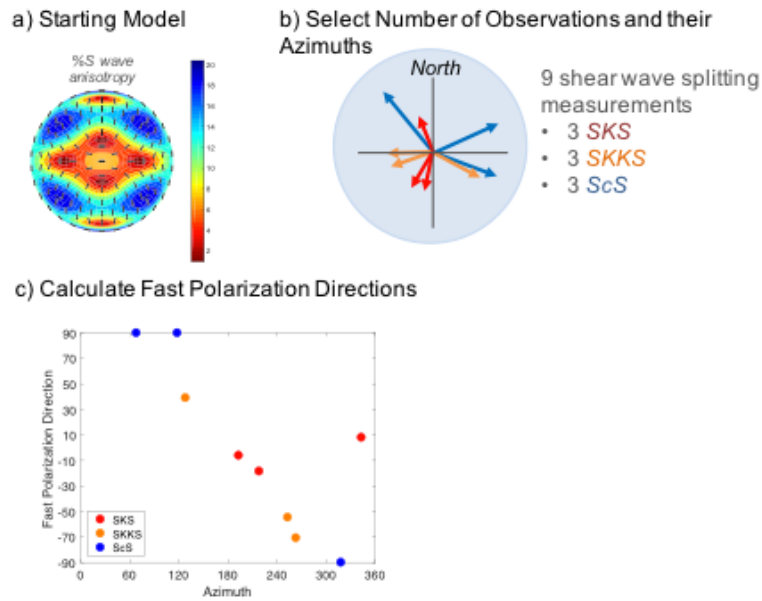
841 Figure 4. Flow chart of steps in our modeling framework. The first step is to identify
 842 the starting model and its orientation from Tables 1 or 2. Secondly, randomly choose an
 843 azimuthal distribution of raypaths through the starting model and fix the SKS number.
 844 Thirdly, use the raypaths from step 2 and calculate the fast polarization directions and/or
 845 reflection polarities (splitting parameters) based on the identified starting model and SKS

1
2
3 846 number. Fourth, use this synthetic dataset to use the forward modeling approach to identify
4
5 847 which models and orientations fit the synthetic dataset. We apply the misfit cutoff as
6
7 848 described in Methods to eliminate certain models and orientations in order to see if the
8
9 849 synthetic dataset can uniquely constrain the starting model. Lastly, in step 5, we repeat this
10
11 850 same process M times (number of iterations), identifying a new random distribution of
12
13
14
15 851 raypaths each time.



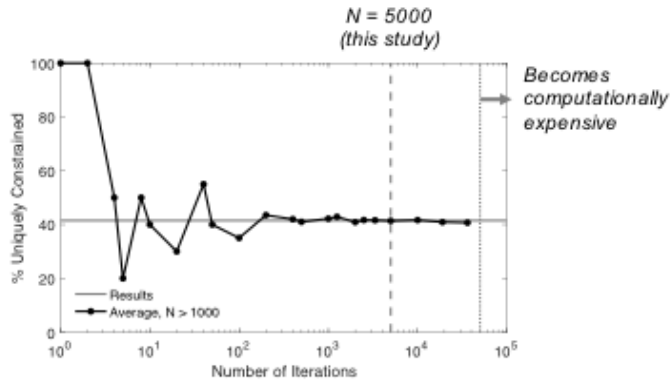
32
33 852

34
35 853 Figure 5. An illustrative example of how shear wave splitting predictions for an
36
37 854 individual iteration in our stochastic modeling scheme are calculated. (a) Plane view
38
39 855 (looking down from above on CMB) of starting model for Ppv (Stackhouse et al., 2005)
40
41 856 showing S wave % anisotropy (colors), with fast polarization directions plotted as black
42
43 857 bars. (b) Raypath distribution for this example for SKS (red), SKKS (orange), and ScS
44
45 858 (blue), plotted as azimuth from north. (c) The predicted fast polarization directions based
46
47 859 on the starting model in (a) and the raypath distribution in (b). Colors indicate phase type.



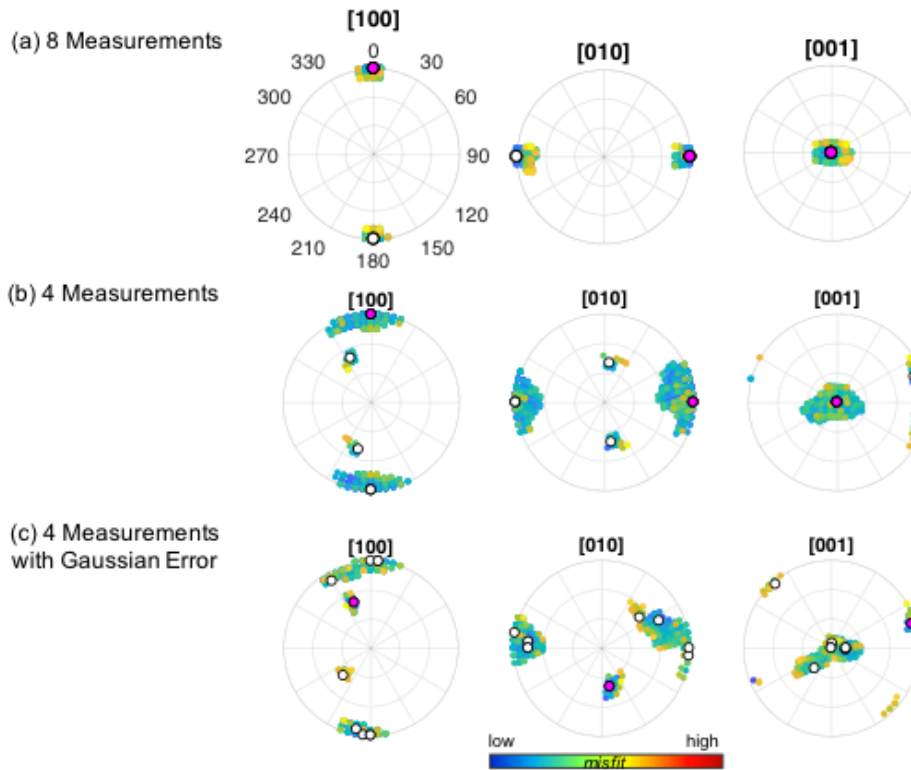
860

861 Figure 6. Results of a test of how many iterations are needed for the model results
 862 to converge. The x-axis defines the number of iterations (M) (that is, number of unique
 863 raypath configurations with similar characteristics) that were successively carried out. The
 864 y-axis indicates what percentage of the iterations run could be uniquely constrained. This
 865 particular test used 9 shear wave splitting measurements and a starting model of horizontal
 866 Ppv, and we found that after a large number of iterations, the starting model could be
 867 constrained for 41% of all iterations carried out. In contrast, for the other 59%, a unique
 868 solution of Ppv could not be constrained for that particular synthetic dataset. Based on the
 869 results of this test, at least 5,000 iterations were carried out for each test described in this
 870 study.



871

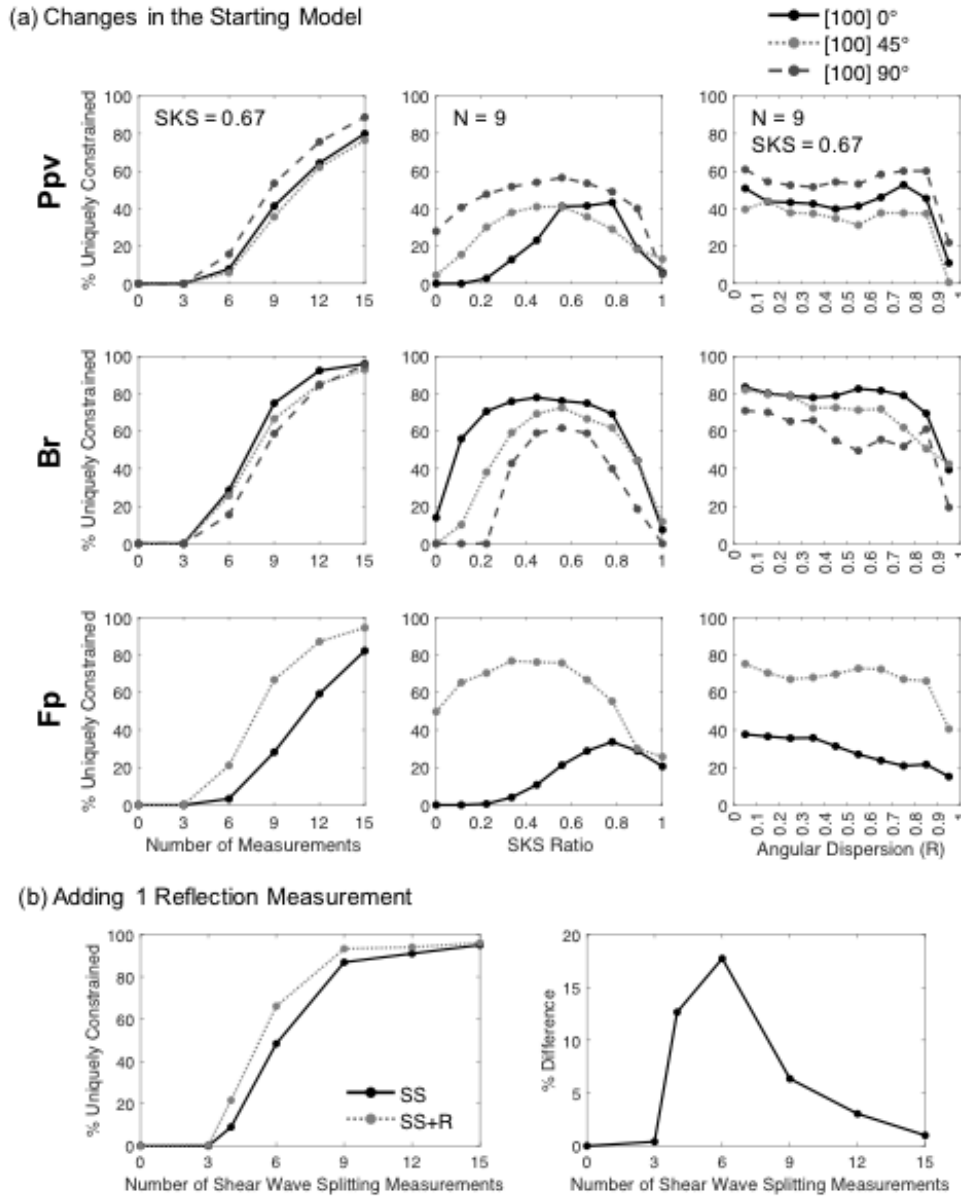
872 Figure 7. An example of how the forward modeling method identifies all possible
 873 orientations of the Ppv single crystal elastic tensor that fit a particular synthetic dataset. We
 874 show two synthetic datasets of 8 (a) and 4 (b) **unique synthetic measurements** with 3 SKS,
 875 3 SKKS, 2 ScS measurements and 1 SKS, 2 SKKS, and 1 ScS measurements, respectively.
 876 The last case (c) shows a test with the same 4 synthetic measurements as in (b) **but with**
 877 Gaussian distributed random error to the predicted fast directions. **These projections show**
 878 all possible permissible orientations (colored dots) of the Ppv tensor for the given synthetic
 879 dataset plotted **as an upper hemispherical projection of the [100], [010], and [001] axes.**
 880 The **white dots** mark local minima, where the magenta **dots** represent the global minimum.
 881 The magenta **dots** indicate the **global** minimum misfit, which should be equal to a non-
 882 rotated Ppv (that is, horizontal [100] **and [010] axes and vertical [001] axis**).



883

884 Figure 8: Results of synthetic tests that aim to uniquely constrain the starting
 885 model/mechanism, as discussed in section 3.2. Three different sets of tensors were tested,
 886 while three different aspects of the raypath configuration were varied. In (a), each row
 887 shows plots of the probability of uniquely identifying the given starting model (Ppv, Br,
 888 and MgO). Each column represents the variable describing raypath configuration that was
 889 allowed to vary, while the other two were fixed. In the first column, we varied the number
 890 of measurements N , but fixed the SKS ratio (0.67) and tested the full range of possible R
 891 values. In the second column, we varied SKS number but fixed the number of
 892 measurements ($N = 9$) and tested the full range of possible R values. In the third column,
 893 we varied the angular dispersion R , but fixed the number of measurements and SKS
 894 number ($N = 9$ and $SKS = 0.6$). We further tested a range of starting orientations for each
 895 starting model (three for Ppv and Br, two for Fp); the labels (0, 45, 90) refer to the rotation

1
2
3 896 angle (in degrees) about the [100] axis from the horizontal. In (b), we chose Model A in
4
5 897 Figure 3 as the starting model and tested whether we could uniquely constrain this starting
6
7 898 model using a combination of shear wave splitting and reflection measurements. For this
8
9
10 899 test, the SKS number was fixed (0.67) and we tested the full range of possible angular
11
12 900 dispersion values. The test shown in (b: left image) compares synthetic datasets with only
13
14 901 shear wave splitting measurements (black line, SS) to those that include splitting plus one
15
16 902 additional reflection measurement for a P and S reflected phase off the D" over a randomly
17
18 903 defined azimuth (gray line, SS+R). The difference in probability between these two raypath
19
20
21 904 configuration scenarios is shown in right image.
22
23
24
25
26
27
28
29
30
31
32
33
34
35
36
37
38
39
40
41
42
43
44
45
46
47
48
49
50
51
52
53
54
55
56
57
58
59
60



905

906

907

908

909

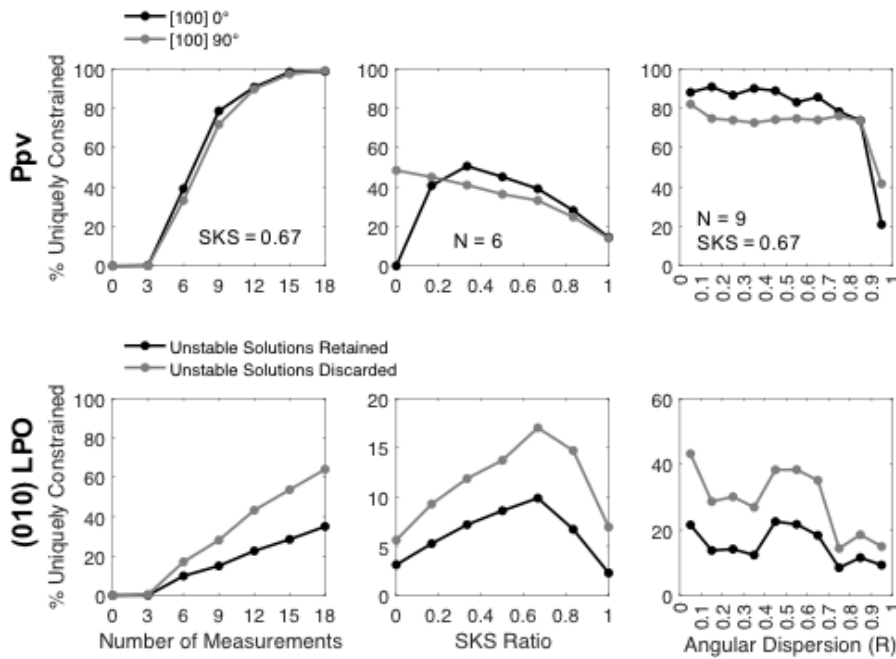
910

911

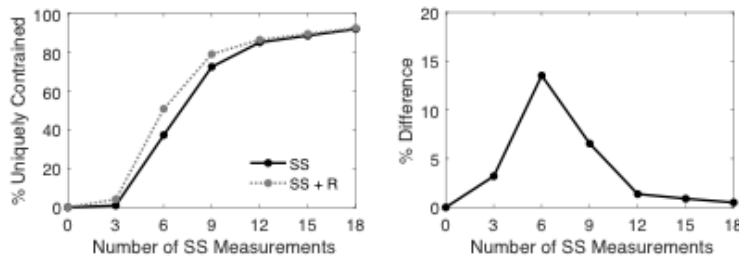
Figure 9. Results of synthetic tests that aim to uniquely constrain the orientation of a Ppv starting model, as discussed in section 3.3. In (a), each row shows plots of the probability of uniquely identifying the given starting model's orientation using the synthetic data, for three different orientations about the [100] axis in the starting model, as shown in the legend (with the labels 0 and 90, referring to the angle about the [100] axis) and described in the text. As in Figure 7, each column represents the variable that was

1
2
3 912 allowed to vary, while the other two were fixed. The second row illustrates the results of
4
5 913 tests that aimed to uniquely constraining the starting model orientation for textured Ppv
6
7 914 models invoking slip on the (010) plane (Walker et al., 2011). For these tests, we
8
9 915 distinguish between scenarios in which we increased the sensitivity (that is, discarded
10
11 916 “unstable” solutions, as described in the text). Tests in which unstable solutions were
12
13 917 discarded (gray line) increased the probability of identifying the orientation of anisotropy
14
15 918 in comparison to retaining unstable solutions (black line). In (b), we show results of tests
16
17 919 of the effect of adding one additional reflection measurement to the shear wave splitting
18
19 920 measurements, using Model A in Figure 3 as the starting model. For these tests, the SKS
20
21 921 number was fixed (0.67) and we tested the full range of possible angular dispersion values.
22
23 922 The test shown in (b: left image) compares synthetic datasets with only shear wave splitting
24
25 923 measurements (black line, SS) to those that include splitting plus one additional reflection
26
27 924 measurement for a P and S reflected phase off the D" over a randomly defined azimuth
28
29 925 (gray line, SS+R). The difference in probability between these two raypath configuration
30
31 926 scenarios is shown at right.
32
33
34
35
36
37
38
39
40
41
42
43
44
45
46
47
48
49
50
51
52
53
54
55
56
57
58
59
60

(a) Changes in the Starting Model Orientation



(b) Adding 1 Reflection Measurement



927

928

929

930

931

932

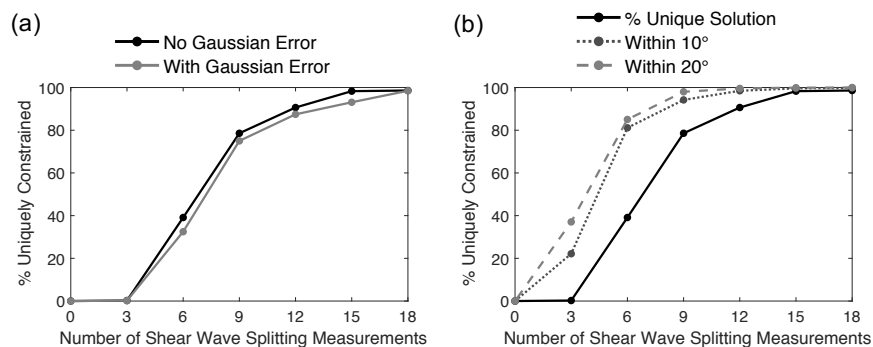
933

934

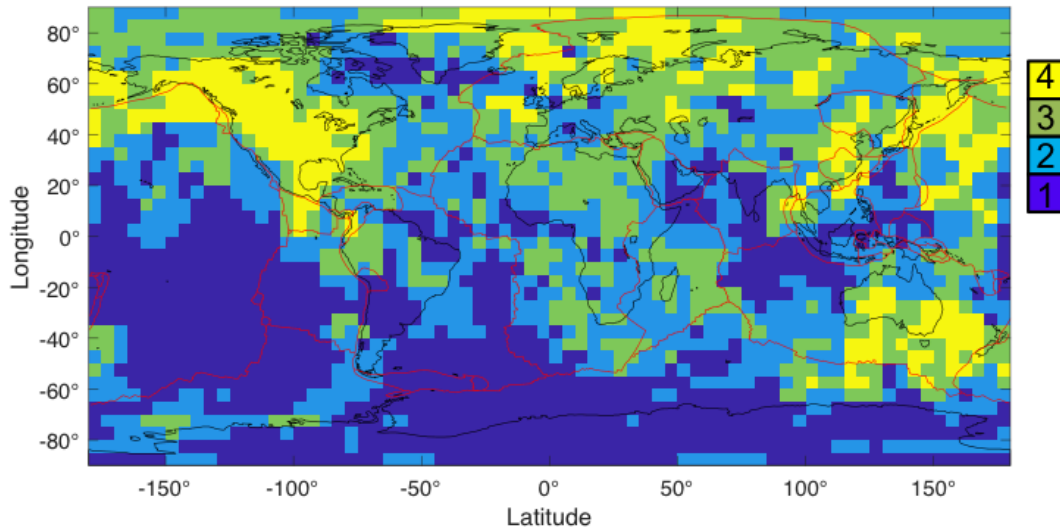
935

Figure 10: Results of tests that aimed to uniquely identify the orientation of a single-crystal Ppv starting model, with Gaussian distributed random errors (standard deviation = 9°) incorporated into the synthetic shear wave splitting dataset. In (a), we varied the number of shear wave splitting measurements and calculated the probabilities of correctly retrieving the starting model orientation. In (b), we plot the probability of correctly identifying the starting orientation for a synthetic dataset with Gaussian error applied based on an identification of the minimum misfit (as opposed to searching for a unique solution). In (b), the black line (unique solution, same as in (a)) shows the probability of uniquely

936 constraining the orientation of the starting model. The other two lines show the probability
 937 of identifying the correct solution within 10° or 20° by using the minimum misfit.



938
 939 Figure 11. Map of regions of the lowermost mantle in which the various
 940 measurement methods (SKS [distance range: $108^\circ - 122^\circ$], SKKS [$108^\circ - 122^\circ$], and ScS
 941 [$60^\circ - 80^\circ$] shear wave splitting and reflection polarities) used in this study could
 942 potentially be applied. We parameterize the D'' layer into a 5° by 5° grid. We calculated
 943 raypaths for different seismic phases using TauP (Crotwell et al., 1999) assuming a 250km
 944 thick D'' layer. We used a set of seismic stations with simple upper mantle anisotropy
 945 (Lynner and Long, 2013, 2014b) for all events greater than Mw6.5 that occurred in the
 946 time span of deployment for each seismic station for SKS, SKKS, and ScS. For reflection
 947 polarities, we considered only dense arrays openly available: TAMNNET, POLENET,
 948 GAMSEIS, Yellowknife Array, KNET, Southern California Network, GRSN Array, F-
 949 Net, USArray (using stations in Alaska), USArray (using stations in Texas), USArray
 950 (using stations in Minnesota), USArray (using stations in New York), USArray (using
 951 stations in South Carolina), and the Pacific Northwest Seismic Network.



952

953 Acknowledgements

954 This work was supported by a National Science Foundation (NSF) Graduate Research
955 Fellowship grant DGE-1122492 to N.C. and by NSF grant EAR-1547499 to M.D.L. Some
956 figures were prepared using the Generic Mapping Tools (Wessel and Smith, 1991). We
957 thank the Yale Center for Research Computing for guidance and use of the research
958 computing infrastructure, specifically Kaylea Nelson. AP received funding from the
959 European Union's Horizon 2020 research and innovation program under the Marie
960 Sklodowska-Curie grant agreement No 642029 - ITN CREEP. We are grateful to Sanne
961 Cottaar and Jeroen Ritsema for thoughtful and constructive reviews that helped us to
962 improve the paper.

963

964

965 **References**

- 966
- 967 Bendat, J.S., Piersol, A.G., 2011. *Random Data: Analysis and Measurement Procedures*.
968 John Wiley & Sons.
- 969 Cottaar, S., Romanowicz, B., 2013. Observations of changing anisotropy across the
970 southern margin of the African LLSVP. *Geophys. J. Int.* ggt285.
971 <https://doi.org/10.1093/gji/ggt285>
- 972 Creasy, N., Long, M.D., Ford, H.A., 2017. Deformation in the lowermost mantle beneath
973 Australia from observations and models of seismic anisotropy. *J. Geophys. Res.*
974 *Solid Earth* 122, 2016JB013901. <https://doi.org/10.1002/2016JB013901>
- 975 Crotwell, H.P., Owens, T.J., Ritsema, J., 1999. The TauP Toolkit: Flexible Seismic
976 Travel-time and Ray-path Utilities. *Seismol. Res. Lett.* 70, 154–160.
977 <https://doi.org/10.1785/gssrl.70.2.154>
- 978 Deng, J., Long, M.D., Creasy, N., Wagner, L., Beck, S., Zandt, G., Tavera, H., Minaya,
979 E., 2017. Lowermost mantle anisotropy near the eastern edge of the Pacific
980 LLSVP: constraints from SKS–SKKS splitting intensity measurements. *Geophys.*
981 *J. Int.* 210, 774–786. <https://doi.org/10.1093/gji/ggx190>
- 982 Ford, H.A., Long, M.D., 2015. A regional test of global models for flow, rheology, and
983 seismic anisotropy at the base of the mantle. *Phys. Earth Planet. Inter.* 245, 71–75.
984 <https://doi.org/10.1016/j.pepi.2015.05.004>
- 985 Ford, H.A., Long, M.D., He, X., Lynner, C., 2015. Lowermost mantle flow at the eastern
986 edge of the African Large Low Shear Velocity Province. *Earth Planet. Sci. Lett.*
987 420, 12–22. <https://doi.org/10.1016/j.epsl.2015.03.029>
- 988 Ford R., Garnero Edward J., McNamara Allen K., 2006. A strong lateral shear velocity
989 gradient and anisotropy heterogeneity in the lowermost mantle beneath the
990 southern Pacific. *J. Geophys. Res. Solid Earth* 111.
991 <https://doi.org/10.1029/2004JB003574>
- 992 Garnero, E.J., McNamara, A.K., Shim, S.-H., 2016. Continent-sized anomalous zones
993 with low seismic velocity at the base of Earth’s mantle. *Nat. Geosci.* 9, 481–489.
994 <https://doi.org/10.1038/ngeo2733>
- 995 Goryaeva, A.M., Carrez, P., Cordier, P., 2017. Modeling defects and plasticity in
996 MgSiO_3 post-perovskite: Part 3—Screw and edge [001]
997 dislocations. *Phys. Chem. Miner.* 44, 521–533. [https://doi.org/10.1007/s00269-](https://doi.org/10.1007/s00269-017-0879-0)
998 017-0879-0
- 999 Groos, J.C., Ritter, J.R.R., 2009. Time domain classification and quantification of seismic
1000 noise in an urban environment. *Geophys. J. Int.* 179, 1213–1231.
1001 <https://doi.org/10.1111/j.1365-246X.2009.04343.x>
- 1002 Guest, W.S., Kendall, J.M., 1993. Modeling seismic waveforms in anisotropic media
1003 using maslov asymptotic theory. *J. Explor. Geophys.* 29, 78–92.
- 1004 Kárasón, H., Hilst, R.D. van der, 2001. Tomographic imaging of the lowermost mantle
1005 with differential times of refracted and diffracted core phases (PKP, Pdiff). *J.*
1006 *Geophys. Res. Solid Earth* 106, 6569–6587.
1007 <https://doi.org/10.1029/2000JB900380>

- 1
2
3 1008 Karki, B.B., Wentzcovitch, R.M., Gironcoli, S. de, Baroni, S., 1999. First-Principles
4 1009 Determination of Elastic Anisotropy and Wave Velocities of MgO at Lower
5 1010 Mantle Conditions. *Science* 286, 1705–1707.
6 1011 <https://doi.org/10.1126/science.286.5445.1705>
7
8 1012 Kawai, K., Geller, R.J., 2010. The vertical flow in the lowermost mantle beneath the
9 1013 Pacific from inversion of seismic waveforms for anisotropic structure. *Earth*
10 1014 *Planet. Sci. Lett.* 297, 190–198. <https://doi.org/10.1016/j.epsl.2010.05.037>
11 1015 Kendall, J.-M., Silver, P.G., 1998. Investigating Causes of D'' Anisotropy, in: *The Core-*
12 1016 *Mantle Boundary Region*. American Geophysical Union, Washington D.C., pp.
13 1017 409–412.
14
15 1018 Lay T., Helmberger D.V., 1983. The shear-wave velocity gradient at the base of the
16 1019 mantle. *J. Geophys. Res. Solid Earth* 88, 8160–8170.
17 1020 <https://doi.org/10.1029/JB088iB10p08160>
18 1021 Lee, K.K.M., O'Neill, B., Panero, W.R., Shim, S.-H., Benedetti, L.R., Jeanloz, R., 2004.
19 1022 Equations of state of the high-pressure phases of a natural peridotite and
20 1023 implications for the Earth's lower mantle. *Earth Planet. Sci. Lett.* 223, 381–393.
21 1024 <https://doi.org/10.1016/j.epsl.2004.04.033>
22
23 1025 Long Maureen D., Lynner Colton, 2015. Seismic anisotropy in the lowermost mantle
24 1026 near the Perm Anomaly. *Geophys. Res. Lett.* 42, 7073–7080.
25 1027 <https://doi.org/10.1002/2015GL065506>
26
27 1028 Long, M.D., 2009. Complex anisotropy in D'' beneath the eastern Pacific from SKS–
28 1029 SKKS splitting discrepancies. *Earth Planet. Sci. Lett.* 283, 181–189.
29 1030 <https://doi.org/10.1016/j.epsl.2009.04.019>
30 1031 Long, M.D., Xiao, X., Jiang, Z., Evans, B., Karato, S., 2006. Lattice preferred orientation
31 1032 in deformed polycrystalline (Mg,Fe)O and implications for seismic anisotropy in
32 1033 D'' . *Phys. Earth Planet. Inter.* 156, 75–88.
33 1034 <https://doi.org/10.1016/j.pepi.2006.02.006>
34
35 1035 Lynner, C., Long, M.D., 2014a. Lowermost mantle anisotropy and deformation along the
36 1036 boundary of the African LLSVP. *Geophys. Res. Lett.* 41, 2014GL059875.
37 1037 <https://doi.org/10.1002/2014GL059875>
38 1038 Lynner, C., Long, M.D., 2014b. Sub-slab anisotropy beneath the Sumatra and circum-
39 1039 Pacific subduction zones from source-side shear wave splitting observations.
40 1040 *Geochem. Geophys. Geosystems* 15, 2262–2281.
41 1041 <https://doi.org/10.1002/2014GC005239>
42
43 1042 Lynner, C., Long, M.D., 2013. Sub-slab seismic anisotropy and mantle flow beneath the
44 1043 Caribbean and Scotia subduction zones: Effects of slab morphology and
45 1044 kinematics. *Earth Planet. Sci. Lett.* 361, 367–378.
46 1045 <https://doi.org/10.1016/j.epsl.2012.11.007>
47
48 1046 Mardia, K.V., Jupp, P.E., 2000. *Directional statistics*. Wiley.
49 1047 McNamara, A.K., Karato, S.-I., van Keken, P.E., 2001. Localization of dislocation creep
50 1048 in the lower mantle: implications for the origin of seismic anisotropy. *Earth*
51 1049 *Planet. Sci. Lett.* 191, 85–99. [https://doi.org/10.1016/S0012-821X\(01\)00405-8](https://doi.org/10.1016/S0012-821X(01)00405-8)
52 1050 Meade, C., Silver, P.G., Kaneshima, S., 1995. Laboratory and seismological observations
53 1051 of lower mantle isotropy. *Geophys. Res. Lett.* 22, 1293–1296.
54 1052 <https://doi.org/10.1029/95GL01091>
55
56
57
58
59
60

- 1
2
3 1053 Mitrovica, J.X., Forte, A.M., 2004. A new inference of mantle viscosity based upon joint
4 1054 inversion of convection and glacial isostatic adjustment data. *Earth Planet. Sci.*
5 1055 *Lett.* 225, 177–189. <https://doi.org/10.1016/j.epsl.2004.06.005>
6 1056 Murakami, M., Hirose, K., Kawamura, K., Sata, N., Ohishi, Y., 2004. Post-Perovskite
7 1057 Phase Transition in MgSiO₃. *Science* 304, 855–858.
8 1058 <https://doi.org/10.1126/science.1095932>
9 1059 Nowacki, A., Wookey, J., 2016. The limits of ray theory when measuring shear wave
10 1060 splitting in the lowermost mantle with ScS waves. *Geophys. J. Int.* 207, 1573–
11 1061 1583. <https://doi.org/10.1093/gji/ggw358>
12 1062 Nowacki, A., Wookey, J., Kendall, J.-M., 2011. New advances in using seismic
13 1063 anisotropy, mineral physics and geodynamics to understand deformation in the
14 1064 lowermost mantle. *J. Geodyn.* 52, 205–228.
15 1065 <https://doi.org/10.1016/j.jog.2011.04.003>
16 1066 Nowacki, A., Wookey, J., Kendall, J.-M., 2010. Deformation of the lowermost mantle
17 1067 from seismic anisotropy. *Nature* 467, 1091–1094.
18 1068 <https://doi.org/10.1038/nature09507>
19 1069 Parisi, L., Ferreira, A.M.G., Ritsema, J., 2018. Apparent Splitting of S Waves
20 1070 Propagating Through an Isotropic Lowermost Mantle. *J. Geophys. Res. Solid*
21 1071 *Earth* 123. <https://doi.org/10.1002/2017JB014394>
22 1072 Simmons, N.A., Forte, A.M., Boschi, L., Grand, S.P., 2010. GyPSuM: A joint
23 1073 tomographic model of mantle density and seismic wave speeds. *J. Geophys. Res.*
24 1074 *Solid Earth* 115, B12310. <https://doi.org/10.1029/2010JB007631>
25 1075 Simmons, N.A., Forte, A.M., Grand, S.P., 2009. Joint seismic, geodynamic and mineral
26 1076 physical constraints on three-dimensional mantle heterogeneity: Implications for
27 1077 the relative importance of thermal versus compositional heterogeneity. *Geophys.*
28 1078 *J. Int.* 177, 1284–1304. <https://doi.org/10.1111/j.1365-246X.2009.04133.x>
29 1079 Simmons, N.A., Myers, S.C., Johannesson, G., Matzel, E., Grand, S.P., 2015. Evidence
30 1080 for long-lived subduction of an ancient tectonic plate beneath the southern Indian
31 1081 Ocean. *Geophys. Res. Lett.* 42, 2015GL066237.
32 1082 <https://doi.org/10.1002/2015GL066237>
33 1083 Stackhouse, S., Brodholt, J.P., Wookey, J., Kendall, J.-M., Price, G.D., 2005. The effect
34 1084 of temperature on the seismic anisotropy of the perovskite and post-perovskite
35 1085 polymorphs of MgSiO₃. *Earth Planet. Sci. Lett.* 230, 1–10.
36 1086 <https://doi.org/10.1016/j.epsl.2004.11.021>
37 1087 Thomas, C., Wookey, J., Brodholt, J., Fieseler, T., 2011a. Anisotropy as cause for
38 1088 polarity reversals of D'' reflections. *Earth Planet. Sci. Lett.* 307, 369–376.
39 1089 <https://doi.org/10.1016/j.epsl.2011.05.011>
40 1090 Thomas, C., Wookey, J., Simpson M., 2007. D'' anisotropy beneath Southeast Asia.
41 1091 *Geophys. Res. Lett.* 34. <https://doi.org/10.1029/2006GL028965>
42 1092 Walker, A.M., Forte, A.M., Wookey, J., Nowacki, A., Kendall, J.-M., 2011. Elastic
43 1093 anisotropy of D'' predicted from global models of mantle flow. *Geochem.*
44 1094 *Geophys. Geosystems* 12, Q10006. <https://doi.org/10.1029/2011GC003732>
45 1095 Walker, A.M., Wookey, J., 2012. MSAT—A new toolkit for the analysis of elastic and
46 1096 seismic anisotropy. *Comput. Geosci.* 49, 81–90.
47 1097 <https://doi.org/10.1016/j.cageo.2012.05.031>
48
49
50
51
52
53
54
55
56
57
58
59
60

- 1
2
3 1098 Walte, N.P., Heidelbach, F., Miyajima, N., Frost, D.J., Rubie, D.C., Dobson, D.P., 2009.
4 1099 Transformation textures in post-perovskite: Understanding mantle flow in the D
5 1100 " layer of the Earth. *Geophys. Res. Lett.* 36, L04302.
6 1101 <https://doi.org/10.1029/2008GL036840>
7 1102 Wang, Y., Wen, L., 2007. Geometry and P and S velocity structure of the "African
8 1103 Anomaly." *J. Geophys. Res. Solid Earth* 112, B05313.
9 1104 <https://doi.org/10.1029/2006JB004483>
10 1105 Wentzcovitch, R.M., Tsuchiya, T., Tsuchiya, J., 2006. MgSiO₃ postperovskite at D"
11 1106 conditions. *Proc. Natl. Acad. Sci. U. S. A.* 103, 543–546.
12 1107 <https://doi.org/10.1073/pnas.0506879103>
13 1108 Wookey, J., Kendall, J.-M., 2008. Constraints on lowermost mantle mineralogy and
14 1109 fabric beneath Siberia from seismic anisotropy. *Earth Planet. Sci. Lett.* 275, 32–
15 1110 42. <https://doi.org/10.1016/j.epsl.2008.07.049>
16 1111 Wookey, J., Kendall, J.-M., Rumpker, G., 2005a. Lowermost mantle anisotropy beneath
17 1112 the north Pacific from differential S—ScS splitting. *Geophys. J. Int.* 161, 829–
18 1113 838. <https://doi.org/10.1111/j.1365-246X.2005.02623.x>
19 1114 Wookey, J., Stackhouse, S., Kendall, J.-M., Brodholt, J., Price, G.D., 2005b. Efficacy of
20 1115 the post-perovskite phase as an explanation for lowermost-mantle seismic
21 1116 properties. *Nature* 438, 1004–1007. <https://doi.org/10.1038/nature04345>
22 1117 Yamazaki, D., Yoshino, T., Ohfuji, H., Ando, J., Yoneda, A., 2006. Origin of seismic
23 1118 anisotropy in the D" layer inferred from shear deformation experiments on post-
24 1119 perovskite phase. *Earth Planet. Sci. Lett.* 252, 372–378.
25 1120 <https://doi.org/10.1016/j.epsl.2006.10.004>
26 1121
27
28
29
30
31
32
33
34
35
36
37
38
39
40
41
42
43
44
45
46
47
48
49
50
51
52
53
54
55
56
57
58
59
60

Supplemental Material:**Constraining lowermost mantle anisotropy with body waves: A synthetic modeling study**

Neala Creasy^{1*}, Angelo Pisconti², Maureen D. Long¹, Christine Thomas², and James Wookey³

¹Department of Geology and Geophysics, Yale University

²Institut für Geophysik, Universität Münster

³Department of Earth Sciences, University of Bristol

*Corresponding author. Email: neala.creasy@yale.edu

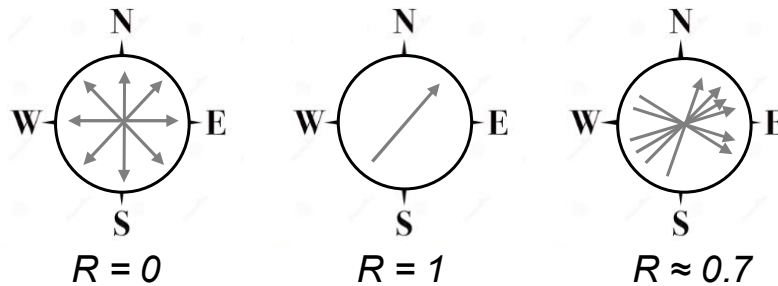
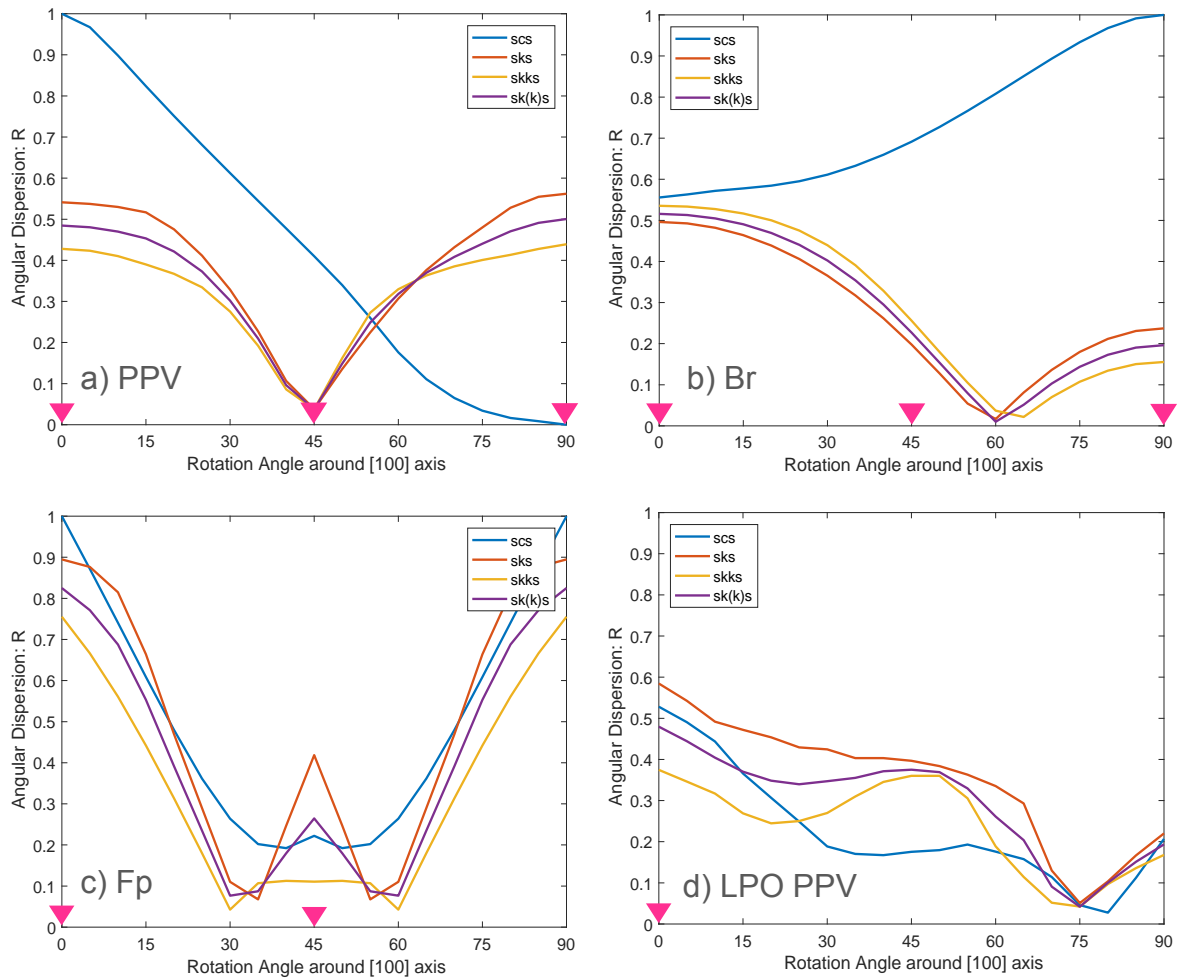
Supplement Figures

Figure S1. Schematic diagram showing the definition of angular dispersion (R), with arrows indicating a direction anywhere from 0° to 360° . Small values of R indicate a wide distribution of directions, while larger values indicate a tight configuration.

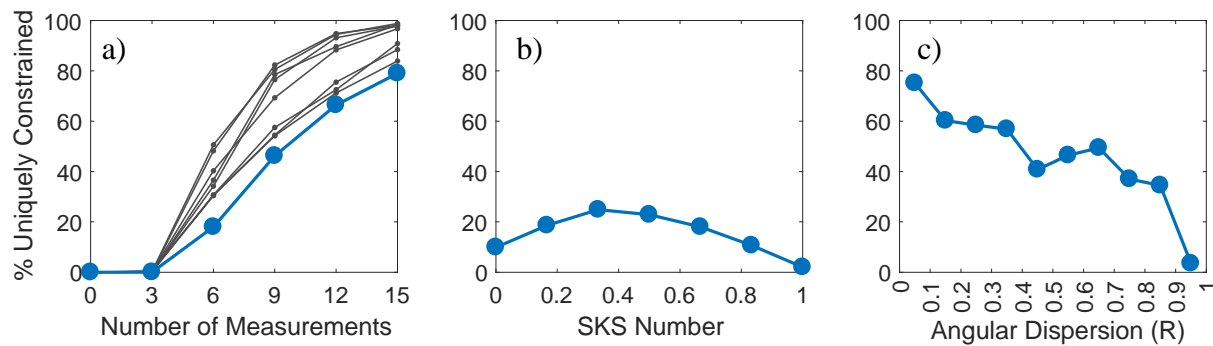


21

22

23 Figure S2. Angular dispersion – R – plots of all predicted fast axis directions for SKS (red),
 24 SKKS (orange), SKS and SKKS (violet), and ScS (blue). Equations (2) and (3) from the main text
 25 were used to calculate R; however, since fast axis directions can only vary from -90° to 90° , the
 26 fast axis orientations were adjusted from -90 to 90 to 0 to 360 . Angular dispersion is plotted in
 27 terms of the clockwise rotation angle about the [100] axis of (a) post-perovskite (PPV), (b)
 28 bridgmanite (Br), (c) ferropericlase (Fp), and (d) LPO of PPV of the given models, respectively.
 29 Magenta triangles indicate the starting models' orientations used in the modeling in the main text
 30 as in Figures 8 and 9.

31



32

33

34 Figure S3. Results of synthetic tests that aim to uniquely constrain the orientation of a Ppv
 35 starting model, as discussed in section 3.3 in the main text, by selecting 9 random the starting
 36 orientations of the Ppv tensor. Each figure illustrates the probability of uniquely identifying the
 37 given starting model's orientation using the synthetic data, for nine different orientations of Ppv.
 38 As in Figure 7, each column represents the variable that was allowed to vary, while the other two
 39 were fixed. For (a), the SKS number was fixed (0.67). For (b), the number of measurements was
 40 fixed to six. For (c), the number of measurements was fixed to nine measurements and an SKS
 41 number of 0.67. The blue lines in (b) and (c) correlate to the blue line in (a), where the variation
 42 of SKS number and angular dispersion were only tested for one of the starting model orientations.

43

44

45

46

47

48

49

50

51

52

53

54

55

56

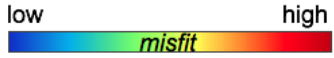
57

58

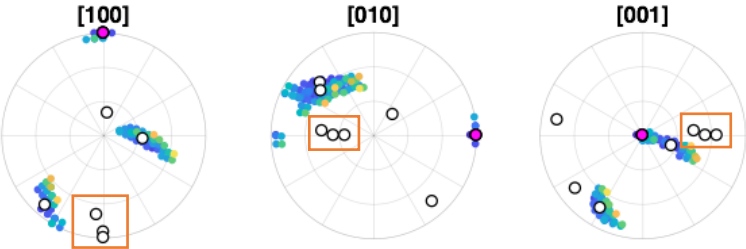
59

60

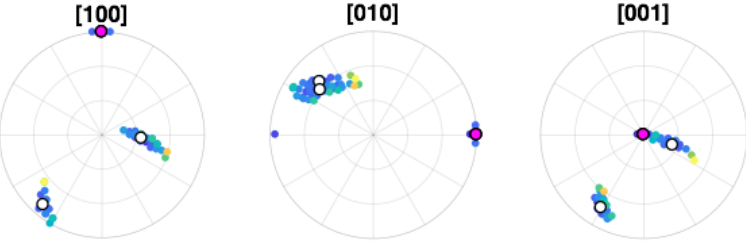
1
2
3
4
5
6
7
8
9
10
11
12
13
14
15
16
17
18
19
20
21
22
23
24
25
26
27
28
29
30
31
32
33
34
35
36
37
38
39
40
41
42
43
44
45
46
47
48
49
50
51
52
53
54
55
56
57
58
59
60



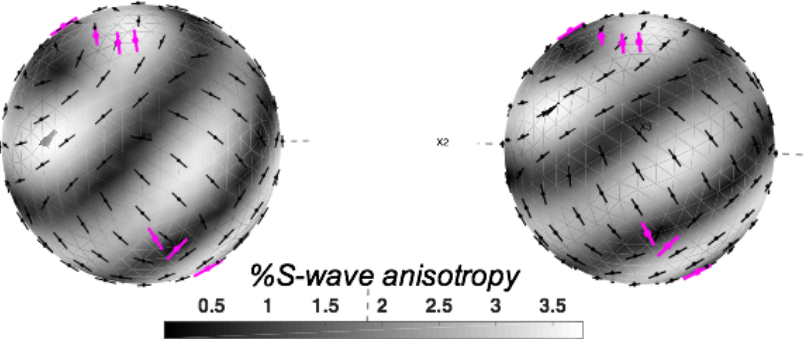
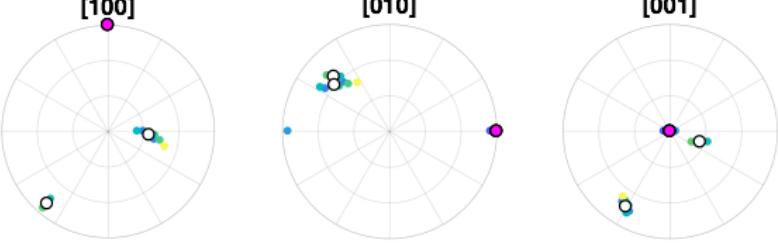
Cutoff = 20°



Cutoff = 15°



Cutoff = 10°



Unstable solution

Unstable solution rotated by 5 degrees, which fails the misfit criterion

45

46

47

48

1
2
3 49 Figure S4: Example illustrating the identification of unstable solutions in a test that aimed
4
5 50 to identify the starting orientation of a horizontal textured Ppv LPO. The polar plots show all
6
7 51 possible orientations that fit a given synthetic dataset. The colors represent misfit values. The white
8
9 52 circles mark the minimum misfit of each cluster of possible orientations. The magenta circles show
10
11 53 the correct solution. The orange boxes highlight some of the unstable solutions. Each row
12
13 54 represents a different misfit cutoff. The top row represents the cutoff used in this study (20°). The
14
15 55 second row uses a cutoff of 15° and the third row 10° . With a lower cutoff, the unstable solutions
16
17 56 are eliminated. The bottom elastic tensors on the left show an example of one of the resulting
18
19 57 unstable solution from the orange boxes in the first row. The elastic tensor on the right shows the
20
21 58 same tensor but rotated by 5° , which fails the misfit criterion. The magenta lines represent the
22
23 59 measurements used in this simulation. Colors here represent %S wave anisotropy.
24
25
26
27
28
29
30
31
32
33
34
35
36
37
38
39
40
41
42
43
44
45
46
47
48
49
50
51
52
53
54
55
56
57
58
59
60